CHALMERS
UNIVERSITY OF TECHNOLOGY

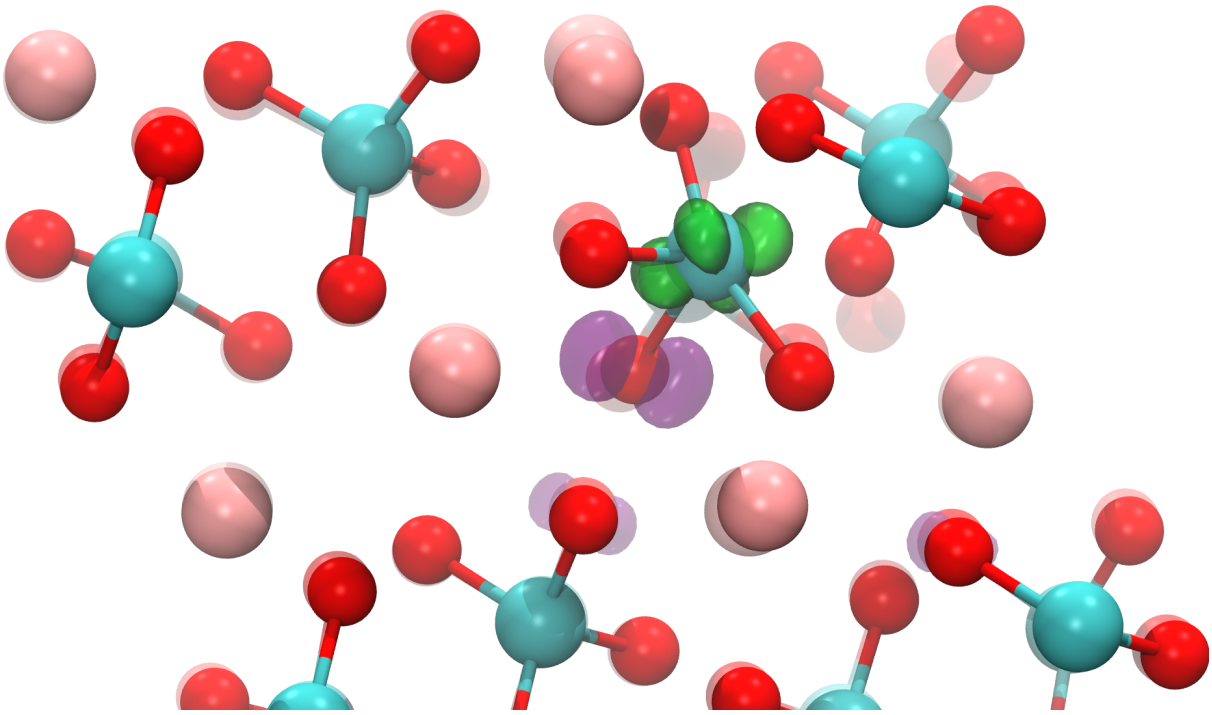

Self-trapped excitons at the surface of $BiVO_4$

A computational investigation on charge localisation at the material-vacuum interface

Master's thesis in Complex Adaptive Systems

Olle Lyth Andersson

DEPARTMENT OF PHYSICS
CHALMERS UNIVERSITY OF TECHNOLOGY
Gothenburg, Sweden 2025
www.chalmers.se

MASTER'S THESIS 2025

Self-trapped excitons at the surface of $BiVO_4$

A computational investigation on charge localisation at the material-vacuum interface

OLLE LYTH ANDERSSON

CHALMERS
UNIVERSITY OF TECHNOLOGY

Department of Physics
Division of Condensed Matter and Materials Theory
Wiktor group
CHALMERS UNIVERSITY OF TECHNOLOGY
Gothenburg, Sweden 2025

Self-trapped excitons at the surface of $BiVO_4$
A computational investigation on charge localisation at the material-vacuum interface
OLLE LYTH ANDERSSON

Supervisor: Tobias Möslinger, Department of Physics
Examiner: Julia Wiktor, Department of Physics

Master's Thesis 2025
Department of Physics
Division of Condensed Matter and Materials Theory
Wiktor group
Chalmers University of Technology
SE-412 96 Gothenburg
Telephone +46 31 772 1000

Cover: Visualisation constructed in VMD showing a self-trapped exciton localising near the vacuum interface of a skewed $BiVO_4$ surface-structure.

Typeset in LaTeX
Printed by Chalmers Reproservice
Gothenburg, Sweden 2025

Self-trapped excitons in the surface of $BiVO_4$
A computational investigation on charge localisation at the material-vacuum interface

OLLE LYTH ANDERSSON
Department of Physics
Chalmers University of Technology

Abstract

In recent years, $BiVO_4$ has emerged as one of the most promising photocatalysts for use in solar-driven water-splitting applications. Its favourable placement of band edges close to the redox potentials of water, together with the physical stability of the material, makes it stand out from many of its competitors. However, previous studies have demonstrated that the bulk structure of $BiVO_4$ suffers from considerable charge localisation, with reduced charge mobility and worsened photocatalytic properties as a result. This study aims to continue these investigations by analysing the formation of localised states at the material-vacuum interface. Using hybrid density functional theory, simulations are performed on two different surface structures in order to identify the most commonly appearing charge localisations, as well as compute their respective formation energies. For both surfaces, several different localised states are found, with self-trapped excitons appearing both in the direct vacuum interface and in the layer immediately below. By effectively lowering the band gap of $BiVO_4$, these localisations are shown to potentially hamper the overall capability of the material to drive the redox reaction.

Keywords: solar-driven water splitting, transition metal oxides, bismuth vanadate, charge localisation, self-trapped excitons, vacuum-interface, density functional theory, hybrid functionals.

Acknowledgements

The fulfilment of this thesis has been made possible by a number of different people, and I would like to express my sincere gratitude to all of you who have supported me during my last semester here at Chalmers University of Technology.

First of all, I would like to thank Julia Wiktor for being a most gracious examiner, and for helping me formulate this project. If not for your absolutely vital input on a number of different things, there would not be much of value to write about in the final report, and I am truly grateful for the opportunity of being part of your research group.

I would also like to thank my supervisor Tobias Möslinger, who has been the subject of many questions throughout these last months. Some of them good, a lot of them maybe less so, but I have nonetheless really enjoyed our discussions about STEs, and the struggles of modifying lattice structures in `VMD`.

Additionally, I say thank you to all the people I have worked with here at the division of Condensed Matter and Materials Theory. It has been a pleasure to fika, laugh and learn from you all in the corridor.

Lastly, I am sending a special thanks to my fellow Master students, at the division and elsewhere, with whom I have shared both adversity and success during these five years of engineering physics. A heartfelt good luck to you all in your future endeavours!

Olle Lyth Andersson, Gothenburg, June 2025

List of Acronyms

Below is the list of acronyms that have been used throughout this thesis listed in alphabetical order:

BOA	Born-Oppenheimer Approximation
CBM	Conduction Band Minimum
COD	Crystallography Open Database
CPU	Central Processing Unit
DFT	Density Functional Theory
GGA	Generalised Gradient Approximation
HER	Hydrogen Evolution Reaction
HPC	High-performance Computing
LDA	Local Density Approximation
OER	Oxygen Evolution Reaction
PES	Potential Energy Surface
RES	Renewable-based Energy Sources
SIE	Self-interaction Error
STE	Self-trapped Exciton
TMO	Transition Metal Oxide

Nomenclature

Below is the nomenclature of notable variables, functions and functionals that have been used throughout this thesis.

Variables

ϵ_{VBM}	Energy of valence band maximum
ϵ_{CBM}	Energy of conduction band minimum
$E_{\text{f}}^{\text{STE}}$	STE formation energy
t	Time
$\mathbf{r}$	Position vector of an electron
$\mathbf{R}$	Position vector of a nucleus
N	Number of particles in a system
Z_n	Atomic number of lattice ion
ϵ_i	Kohn-Sham energy
α	Fraction of exact Hartree-Fock exchange

Functions and functionals

Φ	Wave function of the full condensed system
χ_k	Nuclear eigenfunction to the Schrödinger equation
Ψ_k	Electronic eigenfunction to the Schrödinger equation
ψ_i	Kohn-Sham orbitals
$n(\mathbf{r})$	Electronic density
$V_{\text{ext}}(\mathbf{r})$	External potential of auxiliary system
$\varepsilon_{\text{xc}}[n(\mathbf{r})]$	Exchange-correlation potential functional
$T_0[n(\mathbf{r})]$	Non-interactive energy functional

Contents

List of Figures

1
Introduction

To meet the increasing demands for large scale production of green energy, the exploration of innovative ways to harness power from renewable resources will prove absolutely vital. One prominent field of such research is the utilisation of solar energy as a driving force for desirable reactions. For instance, photochemically induced water splitting using new-generation devices has been shown to hold promising potential as a clean method of producing hydrogen fuel [1]. To sustain this process, which uses the energy of incident sunlight to evolve water molecules into oxygen and hydrogen, transition metal oxides (TMOs) are considered key materials due to their function as photocatalysts and photoelectrodes. Due to the endothermic nature of the reaction, the properties of these TMOs are decisive for the efficiency of the fuel production. The energy required per electron to decompose one water molecule is $1.23\,\mathrm{eV}$ [2]. As a result, the band gap of the TMO needs to be of this value at the very least, generally higher due to systematic energy losses in the physical setup. Furthermore, the band edges should preferably lie outside the redox potentials of water, given that the reaction is driven by free charge carriers in the valence and conduction bands [3, 4]. In addition to possessing these technical capabilities for splitting water, the TMO of course needs to be stable in wet environments and able to absorb a significant part of the incident sunlight. Consequently, the common issue in this field of research often lies in finding a material that combines all of the above properties, since many materials with optimal band gaps instead display unsatisfactory sunlight absorption capacity and vice versa [5].

In recent years, $BiVO_4$ has received considerable attention as a benchmark TMO for water splitting applications due to its favourable light absorption spectrum and positioning of conduction band close to the hydrogen evolution reaction potential [6, 7, 8]. Furthermore, it can also be used to represent a larger class of complex TMOs, making it an ideal choice for studying critical aspects of the reaction [9]. As it stands, a lot of research has been conducted on the bulk properties of $BiVO_4$ and it has been shown to exhibit a band gap of approximately $2.5\,\mathrm{eV}$ [7, 10]. Moreover, its band gap is also close to being direct, enhancing its absorption coefficient [11]. Nonetheless, although these findings remain central for the classification and evaluation of $BiVO_4$ as a potential photocatalyst, a final assessment of the material must include a detailed examination of the properties of the excited charges that drive the redox reactions. The behaviour of excess charges in the bulk, where small polaron formation is well established, has been the subject of numerous studies. Recent experimental work has also indicated the formation of self-trapped excitons STEs, that is, localised electron–hole pairs

stabilised by lattice distortions [12, 13]. However, the properties and dynamics of such excited states at the surface remain far less well understood. Since it is the surface that directly interacts with water in the oxygen evolution reaction, these characteristics will strongly influence reaction efficiency, charge localisation, and material stability — making their investigation essential.

1.1 Self-trapped excitons in $BiVO_4$

The function of a TMO as a photoanode relies on its ability to transport charges through the crystal structure. As free charge carriers are created via the photovoltaic effect, they need to navigate through the lattice and move to the redox site in order to contribute to the reaction. Something previously observed in the bulk of $BiVO_4$ is the creation of polarons in the presence of such free charges [14, 15]. The Coulomb interaction in turn enables these polarons to trap free carriers or other polarons of opposite charge, resulting in the formation of a heavily localised STE. Not only does this significantly inhibit the movement of free charge carriers, it also enables complete recombination due to effective quantum tunnelling [12]. Previous work on $BiVO_4$ has indicated that electron polarons are primarily responsible for hampering the charge transport, something which can be attributed to their large binding energies [12, 16]. Electron-induced lattice deformation seems to occur almost instantly upon excitation, meaning that holes in the valence band remain solely available as units of free charges. In the events that follow however, the holes too tend to localise according to the formation process of STEs described above, impeding the redox reaction even further [16]. In conclusion, the creation of STEs in the crystal structure of $BiVO_4$ is an important phenomenon to account for when investigating new photoanodes. Though they have previously been shown to appear rapidly in the bulk, it remains to be seen if the same behaviour will manifest in the material surface.

1.2 Thesis objective and limitations

The objective of this study is to computationally investigate STEs at the surface of $BiVO_4$. The project aims to provide insights on how surface characteristics modify charge localisation, and how this might affect effectiveness for solar-driven water splitting. Since standard computational methods suffer from the self-interaction error, advanced excited-state methods will be used to explore how surface effects influence the nature and stability of STEs.

One obvious limitation is the lack of prior knowledge about STEs at surface level of the material, which will make it difficult to use optimal configurations right from the start. Therefore, the setup and method will have to be reevaluated and optimised as the work progresses. Moreover, due to the very limited time frame of the project, the calculations will use a code which is comparatively fast but not as accurate as other alternatives. After obtaining initial results, simulations can be made more expensive with other code packages to achieve higher accuracy.

2

Theory

Modern research in condensed matter physics incorporates a variety of disciplines in order to access information about systems on the subatomic level. In addition to making theoretical arguments and physical experiments, numerical simulations play a crucial role in the advancement of our knowledge about materials and crystal structures. Still, the systems under investigation remain incredibly complex. It is practically impossible to directly emulate a larger network of electrons and nuclei due to all the constituent parts interacting in various ways. To enable numerical analysis of condensed matter, one must therefore apply models that simplify the problem, but still manage to describe the system to a satisfactory degree. This chapter will outline the theory and concepts necessary for studying STEs in $BiVO_4$, starting with the formation of polarons and the effects of charge localisation. Then follows a rudimentary description of density functional theory (DFT), a common method of reducing high-dimensional problems to simpler, exactly solvable ones. Lastly, there is an account of the problematic self-interaction error related to classic computational methods, which calls upon the need for advanced excited-state models in place of regular DFT.

2.1 Dynamics of charge carriers

Condensed matter can interact with electromagnetic waves through the photoelectric effect. As incident sunlight is absorbed by the recipient material, electrons are excited from their ground states to occupy states with higher energy. For semiconductor materials, this is commonly described as electrons moving up into the *conduction band*, leaving behind a positively charged hole in the *valence band*. In this way, two delocalised charge carriers have been generated in the crystal structure, which can be transported freely through the lattice. The state corresponding to the highest energy level in the valence band is referred to as the valence band maximum (VBM). Reciprocally, the lowest energy level in the conduction band is denoted as the conduction band minimum (CBM). The difference between these two marks the *band gap* of the material, and is thus the smallest amount of energy needed for the component to become electrically conductive. As such, it is a defining feature for this group of materials. The band gap is said to be *direct* if the CBM can be reached from the VBM without the electron having to absorb any additional momentum. This is a desired quality for many applications, as it enhances the rate of electronic excitation. However, the band gap only marks the smallest possible leap an electron can make. If more

energy is absorbed, states located further up on the valence band, or even other bands of higher energy, can also be attained. Nonetheless, when investigating photoanodes for water-splitting, the smallest transitions in the material are the ones which will prove the most vital.

A special case of the electron acquiring different energies upon excitation is related to its spin-orientation. As the electron absorbs incident sunlight and moves up to a higher orbital, it may do so in a way that either retains the same spin as before, or flips the spin to the opposing orientation, see Fig. 2.1. In the first case, the promoted electron remains in a paired configuration with another electron in the ground state. As such, this state is denoted as a *singlet*, due to the spin-multiplicity being equal to 1. However, if the spin-orientation of the promoted electron flips, a phenomenon enabled by the spin-orbit coupling in quantum systems, the state unpairs itself and thus acquires a multiplicity of 3. Consequently, this state is denoted as a *triplet*. Due to varying screening effects between the paired and unpaired configuration, the triplet state always has a lower energy than the corresponding singlet state, as stipulated by Hund's rule. This means that when researching properties related to the smallest possible transitions in a semiconductor, the excited state should generally be specified as a triplet.

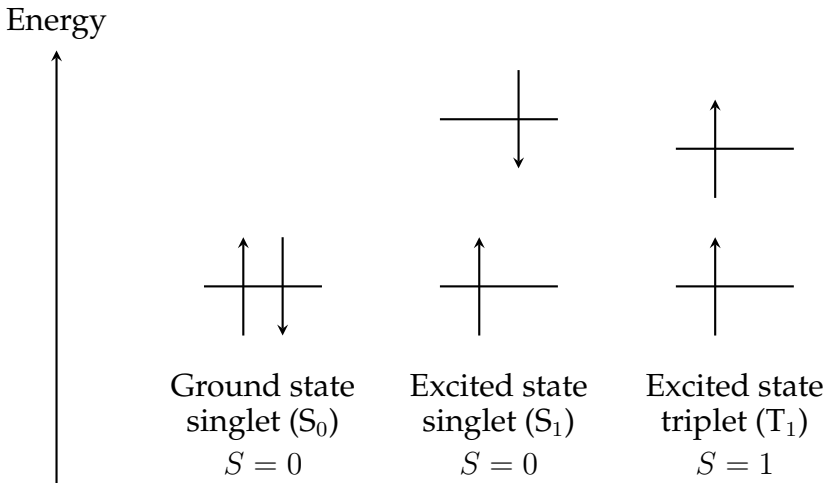

Figure 2.1: Simple graph illustrating the difference between singlet and triplet excitation. If the promoted electron retains its coupling with the ground state electron, the total spin number S remains equal to zero. This leaves only one possible configuration, with total magnetic spin $M_S = 0$. However, if the spin of the promoted electron flips, S will obtain a value of one. This instead enables three possible formations, with total magnetic spin $M_S = \{+1, 0, -1\}$.

2.1.1 The water-splitting reaction

Photochemically driven hydrogen production aims to use the free charges induced from solar excitation to fuel a specific redox reaction. The role of the photoanode is to produce holes and electrons with a certain energy, and transport these to the reaction site. In the case of water splitting, water is first oxidated to

form oxygen gas and hydrogen ions, whereafter hydrogen gas is produced in the ensuing reduction reaction. The process can thus be summarised as:

$$\begin{aligned} 2H_2O &\rightarrow O_2 + 4H^+ + 4e^- \text{ (reduction)}, \\ 4H^+ + 4e^- &\rightarrow 2H_2 \text{ (oxidation)}, \\ 2H_2O &\rightarrow O_2 + 2H_2 \text{ (total reaction)}, \end{aligned} \tag{2.1}$$

where the reduction reaction also is referred to as the oxygen evolution reaction (OER), and the oxidation reaction is known as hydrogen evolution reaction (HER). The energy required per electron in order to split one water molecule is governed by Gibbs Free energy, and is equal to $1.23\,\mathrm{eV}$, regardless of pH [2]. Consequently, to be able to generate charge carriers of sufficient energy, the photocatalyst must have a band gap of this value at the very minimum. Usually, it must be even higher due to the presence of overpotentials in the reaction, causing a discrepancy between the thermodynamically expected reduction potential and the actual value measured experimentally. However, the absolute value of the band gap itself is not enough to drive the reaction. In order for the reaction to occur, the edges of the valence band and the conduction band must straddle the reduction and oxidation potentials of the OER and HER respectively [3]. The exact values of these two potentials do, however, vary with pH, although the difference between them remains constant $1.23\,\mathrm{eV}$. This means that if the effective band gap of the photocatalyst was reduced, for instance by introducing interband states such as polarons, the dynamics would be disrupted and the reaction as a whole may come to a halt.

2.1.2 Formation of localised states

After optical excitation of valence band electrons to the conduction band, the initially delocalised charge carriers can interact with the external nuclei and form small, localised states called polarons. These are usually treated as quasi-particles, emerging from the electric potential of the excess charges inducing a rearrangement of the lattice, see Fig. 2.2. The underlying principle of this phenomenon lies in the intrinsic structure of the crystalline material, as polaronic deformation proves energetically favourable compared to the holes and electrons staying delocalised. This has negative implications for applications as a photocatalyst. Since the charge carriers become trapped in these polaronic states, electric transport in the crystal is slowed down, and its ability to sustain the redox reaction in Eq. 2.1 weakens. However, the exact mechanisms and energies behind polaron formation are different for holes and electrons, and it is possible for one of the two to stay mobile while the other one localises. In $BiVO_4$, electron polarons like the one in Fig. 2.2a have been reported to form almost immediately upon excitation, whereas the holes retain conductivity for longer intervals [12, 16]. Still, holes also form polarons of their own, as seen in Fig. 2.2b. These are usually larger than the electronic ones, and retain a higher overall mobility.

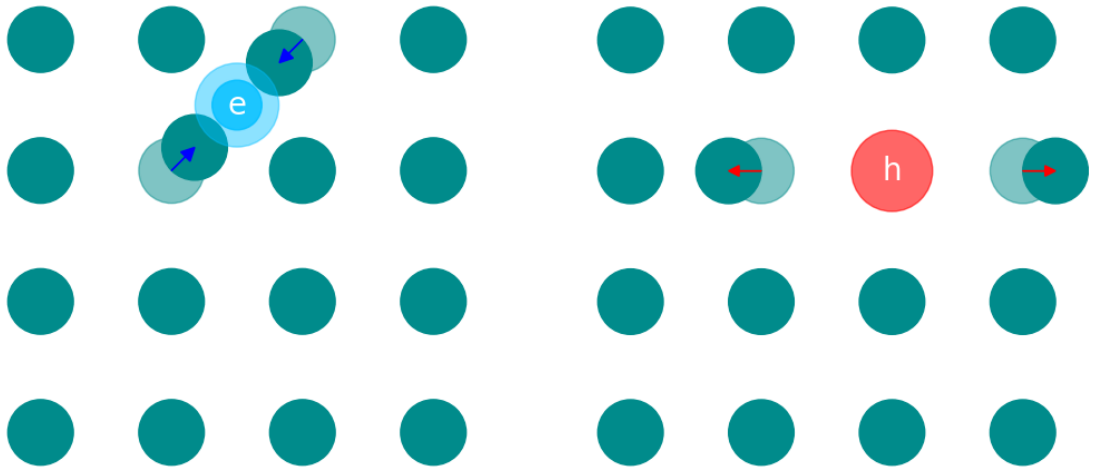

(a) **(b)**

Figure 2.2: Both electrons and holes can localise by rearranging the lattice structure and forming polarons. In order for this to occur, the energy gained though localising must be greater than the energy cost related to deforming the lattice structure. This hampers energy transport in the material, and is therefore a hindrance for solar-driven water splitting. (a) Electronic deformation of the underlying lattice structure. The negatively charged electron attracts positively charged nuclei, generating a small localisation. (b) A positively charged hole can also form polarons, by repelling the external nuclei. This induces a localisation which is slightly bigger than the the electronic one.

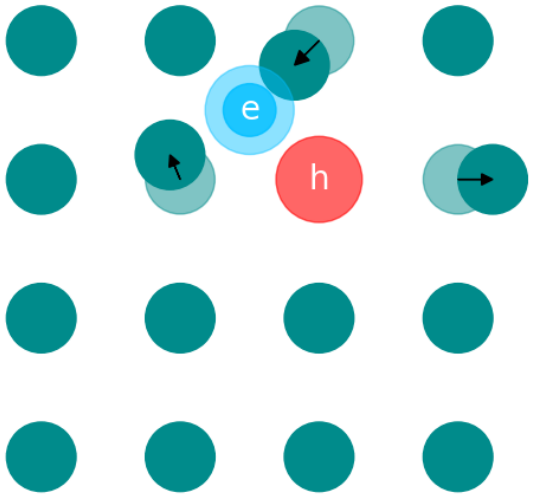

Figure 2.3: The formation of an STE. By combining two polarons of opposite charges, they attract through Coulombic interaction and form a tightly bound electron-hole pair. The result is a localised quasiparticle which also is very stable, consequently slowing down charge transport in the material considerably.

Furthermore, the localisation of either hole or electron enables the creation of another quasi-particle which strengthens localisation. Through Coulomb attraction, a polaron can trap free carriers or other polarons of opposite charge, leading to the formation of the previously mentioned STEs. Just like normal excitons, the STE thus consists of a hole and electron tightly bound together, although they remain trapped due to polaronic interactions with the external lattice, see Fig. 2.3 above. In $BiVO_4$, the overall lattice structure can be described as a constellation of VO_4 units, surrounded by a system of Bi atoms. Previous work within the group has showed that STEs forming in this material tend to either localise around one VO_4 unit, or split up between a VO_4 unit and a Bi atom, see Fig. 3.3. Both of these formations have proved prevalent in the bulk, with similar formation energies in this domain. It remains to be seen which STEs can form at the surface of $BiVO_4$, and if one formation is favoured over the other.

2.1.3 Formation energy and STE stability

The energy of an STE is simply calculated as the difference between the total energy of the crystal including the STE, and the total energy of the crystal at its pristine ground state, that is to say without deformations or excitations. To obtain a measurement of the stability of an STE, the formula is complemented with the band gap of the material according to

$$E_{\mathrm{f}}^{\mathrm{STE}} = E_{\mathrm{total}}^{\mathrm{STE}} - E_{\mathrm{total}}^{\mathrm{GS}} + \epsilon_{\mathrm{VBM}} - \epsilon_{\mathrm{CBM}}, \tag{2.2}$$

where ϵ_{VBM} marks the energy at the VBM and ϵ_{CBM} marks the energy at the CBM. $E_{\mathrm{f}}^{\mathrm{STE}}$ is the so called *formation energy*, and describes the energy of the STE in relation to the fully delocalised states. A positive value of $E_{\mathrm{f}}^{\mathrm{STE}}$ implies that localisation is energetically unfavourable, and that the charge carriers therefore tend to remain conductive. By contrast, a negative value of $E_{\mathrm{f}}^{\mathrm{STE}}$ indicates that the STE-formation lowers the total energy of the system compared to the delocalised configuration. A lower value of $E_{\mathrm{f}}^{\mathrm{STE}}$ thus denotes a more stable STE, which makes the localisation in question more likely to appear. The formation energy is therefore a central measurement for the further characterisation of different STEs.

It is here important to point out the difference between the level of localisation and the stability of an STE. As stated above, the stability of an STE is related to the formation energy, which provides a measurement of how likely the STE is to form based on energetic constraints. On the other hand, the level of localisation is a description of the mobility of the state as a whole. By overcoming a certain energy barrier, individual polarons have previously been demonstrated to move through $BiVO_4$ via a hopping mechanism, and thus managed to resuscitate some of the lost charge mobility in the material [14, 15, 17]. The same holds true for STEs, as they are not completely immobile but rather heavily localised due to a large energy barrier required for lattice hopping. Along with obstructing charge transport in this way, one of the main issues that STEs pose for photoanode materials is the difficulty of separating the electron-hole pair once they have bonded together. As such, this work focuses on examining the stability and formation energies of various STEs, rather than their exact level of localisation.

2.2 Density functional theory

The study of condensed matter concerns how ions and electrons move and interact in a solid structure. As with all quantum mechanical systems, these dynamics can neatly be summarised by the Schrödinger equation, where the wave function in this case is a function of the coordinates of each charged particle according to

$$i\hbar\frac{\partial}{\partial t}\Phi = \hat{H}\Phi(\mathbf{r}_1, \mathbf{r}_2, \mathbf{r}_3, ..., \mathbf{R}_1, \mathbf{R}_2, \mathbf{R}_3 ...; t), \tag{2.3}$$

where $\mathbf{r}_i$ marks the coordinates of the electron indexed i, and $\mathbf{R}_j$ marks the coordinates of the nucleus indexed j. Note that the wave-function Φ also depends parametrically on time. Since the structures are three dimensional, calculating the movement of N particles in such a system becomes a $3N$-dimensional problem. As for the Hamiltonian of the system, it can be divided into three main components. Firstly, there is the kinetic energy of each nucleus, as well as all their respective potential energies arising from interactions with all other nuclei. Then, there is the kinetic energy of each electron, as well as their respective potential energies arising from interactions with all other electrons. Lastly, there is also the potential energy of each particle arising from the mixed interactions between nuclei and electrons. With all of this in mind, the Hamiltonian can be written as

$$\hat{H} = \underbrace{\hat{T}_{\mathbf{R}} + \hat{V}_{\mathbf{R}}}_{\text{nuclear}} + \underbrace{\hat{T}_{\mathbf{r}} + \hat{V}_{\mathbf{r}}}_{\text{electronic}} + \underbrace{\hat{V}_{\mathbf{R},\mathbf{r}}}_{\text{mixed}} \tag{2.4}$$

where $\hat{T}_{\mathbf{R}}$ and $\hat{T}_{\mathbf{r}}$ denote the kinetic energy contributions of the nuclei and electrons respectively, $\hat{V}_{\mathbf{R}}$ and $\hat{V}_{\mathbf{r}}$ represent the potential energies arising from nucleus-nucleus as well as electron-electron interaction, and $\hat{V}_{\boldsymbol{R},\mathbf{r}}$ is the mixed potential which stems from electrons and nuclei interacting with each other.

Due to the complex coupling of subatomic level particles, along with the rapidly increasing degrees of freedom for these systems, computationally investigating the exact Schrödinger equation with sufficient accuracy becomes practically impossible even for small structures. In order to overcome this issue, DFT presents a method that effectively reduces the $3N$-problem to a 3-dimensional one, thus facilitating computational analysis of condensed matter.

2.2.1 The Born-Oppenheimer approximation

The first observation to make is that ions are considerably heavier than electrons. The mass of a single proton outweighs the electron mass by a factor of approximately 1836, which of course causes their dynamics to differ drastically. Due to the higher mass, the lattice ions are far slower than the surrounding electron cloud. Consequently, as the ions move around and cause small perturbations in the lattice, the electrons will react almost instantaneously and rearrange themselves to accommodate the new configuration. The Born-Oppenheimer approximation (BOA) makes use of this fact to simplify the analysis of the system. To a

good estimate, the lattice ions can be considered as fixed in relation to the electrons [18]. This means that the wave function can be separated into electronic and nuclear parts according to

$$\Phi\Big(\{\mathbf{r}_i\}_{i=1}^N, \{\mathbf{R}_j\}_{j=1}^N; t\Big) = \sum_k \Psi_k\Big(\{\mathbf{r}_i\}_{i=1}^N; \{\mathbf{R}_j\}_{j=1}^N\Big)\chi_k\Big(\{\mathbf{R}_j\}_{j=1}^N; t\Big), \tag{2.5}$$

where χ_k is a nuclear many-particle wave-function and Ψ_k is an electronic one. The summation over k stems from expanding the wave function to the complete set of eigenfunctions which satisfy Eq. 2.3 [19]. Note that Ψ_k is parametrically dependent on the nuclei coordinates due to the lattice inducing a static Coulombic potential affecting the electrons. The result of this formulation is that solving the Schrödinger equation becomes a two-step process. By initially viewing the nuclei as fixed, one can solve the equation for the electronic degrees of freedom. Disregarding the nuclear contributions to the Hamiltonian in Eq.2.4, the electronic equation takes the form

$$\begin{aligned}\hat{H}_e\Psi_n\Big(\{\mathbf{r}_i\}_{i=1}^N; \{\mathbf{R}_j\}_{j=1}^N\Big) &= [\hat{T}_\mathbf{r} + \hat{V}_\mathbf{r} + \hat{V}_{\mathbf{r},\boldsymbol{R}}]\Psi_n\Big(\{\mathbf{r}_i\}_{i=1}^N; \{\mathbf{R}_j\}_{j=1}^N\Big) = \\ &= \epsilon\big(\{\mathbf{R}_j\}_{j=1}^N\big)\Psi_n\Big(\{\mathbf{r}_i\}_{i=1}^N; \{\mathbf{R}_j\}_{j=1}^N\Big),\end{aligned} \tag{2.6}$$

where $\hat{H}_e$ marks the electronic Hamiltonian. The term $\epsilon\big(\{\mathbf{R}_j\}_{j=1}^N\big)$ is the total energy of the electronic system, which naturally also depends parametrically on the nuclear positions. Once extracted, this can be used to solve for the nuclear degrees of freedom. By inserting $\epsilon\big(\{\mathbf{R}_j\}_{j=1}^N\big)$ into the nuclear part of the Schrödinger equation, one obtains

$$i\hbar\frac{\partial}{\partial t}\chi_n\Big(\{\mathbf{R}_j\}_{j=1}^N; t\Big) = \Big[\hat{T}_\mathbf{R} + \hat{V}_\mathbf{R} + \epsilon\big(\{\mathbf{R}_j\}_{j=1}^N\big)\Big]\chi_n\Big(\{\mathbf{R}_j\}_{j=1}^N; t\Big), \tag{2.7}$$

which represents a potential energy surface (PES) for χ_n. The nuclear dynamics can be assumed to proceed according to Newton's second law, neglecting quantum mechanical effects. Hence, by utilising the derived PES to optimise the position of the nuclei, one can update the coordinates of the system and reiterate the calculations until convergence is reached.

2.2.2 The Hohenberg-Kohn theorems

The remaining complication with the methodology described above is that solving the electronic part of the Schrödinger equation still is a $3N$-dimensional problem. To enable actual computations, the number of dimensions needs to be reduced. The issue stems from each single electron contributing individually to the total energy of the system. As it stands, the electronic Hamiltonian

$$\hat{H}_e = \hat{T}_\mathbf{r} + \hat{V}_\mathbf{r} + \hat{V}_{\mathbf{r},\boldsymbol{R}} \tag{2.8}$$

has to be applied to the many-particle wave function $\Psi_n\Big(\{\mathbf{r}_i\}_{i=1}^N; \{\mathbf{R}_j\}_{j=1}^N\Big)$, which effectively depends on the coordinates of all constituent particles. In order to

make the whole argument three-dimensional, DFT-algorithms therefore make use of the Hohenberg-Kohn theorems to construct other ways of evaluating the total energy. The idea is to treat the system as if it were under the influence of an external potential $V_{\text{ext}}(\mathbf{r})$, which in turn only depends on the regular three spatial coordinates. This requires reformulating the expressions above so that instead of the individual coordinates for each particle, the calculations are done with regards to the electron density, a simple three dimensional quantity. The first Hohenberg-Kohn theorem suggests how such a derivation can be initialised by relating a general external potential to the electron density of the system [19].

Theorem (Hohenberg-Kohn I)**.** *The external potential $V_{ext}(\boldsymbol{r})$ is determined, within a trivial additive constant, by the electron density $n(\boldsymbol{r})$.*

From this follows an important corollary, namely that since the Hamiltonian is completely determined, the many-body wave-function for the ground state and all excited states must be as well. Consequently, if the ground state electronic density $n_0(\mathbf{r})$ of the system is given, all other properties of the system can be fully inferred from this function alone. As such, finding $n_0(\mathbf{r})$ is a fundamental aspect of DFT. The second Hohenberg-Kohn theorem proceeds to describe how this can be done by optimising a well-defined functional of the density [19].

Theorem (Hohenberg-Kohn II)**.** *For a trial density $\widetilde{n}(\boldsymbol{r})$, such that $\widetilde{n}(\boldsymbol{r}) \geq 0$ and $\int \widetilde{n}(\boldsymbol{r})d\boldsymbol{r} = N$, it holds that $E[n_0] \leq E[\widetilde{n}]$, where n_0 is the ground state electronic density.*

Thus, for any external potential V_{ext}, one can define an energy functional of the density, $E[n(\mathbf{r})]$, such that the global minimum of this functional is given when $n(\mathbf{r})$ equals the exact ground state density $n_0(\mathbf{r})$. This in turn implies that defining this functional is enough to determine the ground state energy and ground state density of the system. Usually the functional is divided up into a universal part and a system dependent part, which includes the contributions from the external potential, according to

$$E[n(\mathbf{r})] = \underbrace{F[n(\mathbf{r})]}_{\text{universal}} + \underbrace{\int V_{\text{ext}}(\mathbf{r})n(\mathbf{r})\mathrm{d}\mathbf{r}}_{\text{system dependent}}. \tag{2.9}$$

The universal functional in turn includes a functional for the kinetic energy, the energy contributions from classical Coulomb interactions between electrons, as well as a correction term for the electronic self-interaction in the system. The last term is non-classical and accounts for the exchange-correlation energy of electronic systems, which will be outlined in detail further down. All in all, the universal functional can thus be written as

$$F[n(\mathbf{r})] = \underbrace{T[n(\mathbf{r})]}_{\text{kinetic}} + \underbrace{\frac{1}{8\pi\varepsilon_0}\int\int \frac{n(\mathbf{r})n(\mathbf{r'})}{\|\mathbf{r}-\mathbf{r'}\|}\mathrm{d}\mathbf{r}\mathrm{d}\mathbf{r'}}_{\text{classic Coulomb}} + E_{\text{xc}}, \tag{2.10}$$

where the correction term for the exchange correlation has been denoted E_{xc}.

2.2.3 The Kohn-Sham equations

Although useful for reducing the dimensionality of the problem, an important note to make about Hohenberg-Kohn theory is that the functional described in Eq. 2.9 often remains undetermined, as there is no direct link between the electron density and kinetic energy of the system. Moreover, the expression for the many-body wave function, and thus the electron density function, also remain unknown. All of this naturally inhibits the construction of a computational algorithm. Real DFT therefore uses the Kohn-Sham approach to enable actual evaluations of the energy levels of the system. The *Kohn-Sham ansatz* builds on the assumption that the ground state energy of an interacting particle system is equal to that of an exactly soluble, non-interacting particle system which instead is subjected to an effective external potential. Consequently, the many-particle wave function Ψ can be treated as separable, and thus be written as the product of all individual electronic wave functions. Denoting these as ψ_i, this takes the mathematical form of

$$\Psi(\boldsymbol{r}_1, \boldsymbol{r}_2, ..., \boldsymbol{r}_N) = \psi_1(\boldsymbol{r}_1)\psi_2(\boldsymbol{r}_2)...\psi_N(\boldsymbol{r}_N), \tag{2.11}$$

an expression commonly known as the *Hartree product*. The anti-symmetric requirement of fermionic systems is fulfilled by taking the Slater determinant of this product, which thus also yields an approximate expression for the wave function. This in turn means that the electron density of a system can be calculated according to

$$n(\mathbf{r}) = \sum_i |\psi_i(\mathbf{r}_i)|^2, \tag{2.12}$$

which is nothing more than superimposing the probability distributions of each individual electron [19]. As such, the Kohn-Sham approach provides a way of describing the electron density function through the individual, non-interacting electronic wave functions, which in general are determined.

Along with providing an expression for the electron density function, Kohn-Sham theory also enables formulation of the previously unknown kinetic energy functional. In contrast to the kinetic energy functional of an interactive system, the kinetic energy functional of an individual, non-interacting particle is commonly known and will here be denoted as $T_0[n(\mathbf{r})]$. Using the expression for total electron density presented above, this can be written as

$$T_0[n(\mathbf{r})] = \int \Big(-\frac{\hbar^2}{2m}\nabla^2 \Big) n(\mathbf{r}) \mathrm{d}\mathbf{r}, \tag{2.13}$$

which simply is the direct kinetic energy for all particles evaluated and superimposed over the whole probability space. In the auxiliary system introduced by Kohn-Sham, evaluation of the kinetic energy is thus enabled by replacing the interactive energy $T[n(\mathbf{r})]$ with the non-interactive energy $T_0[n(\mathbf{r})]$ and using the expression in Eq. 2.13 for computation.

As stipulated by the ansatz, it is now possible to describe the ground state energy of the system in terms of $T_0[n(\mathbf{r})]$, together with an additional effective

potential acting upon the non-interactive system. In this case, the effective potential contains the previously known expressions for external lattice potential and classic Coulomb interaction between electrons, as first shown in Eq. 2.9 and Eq. 2.10 respectively. Additionally, it also includes an approximate energy functional for the previously mentioned exchange-correlation. The resulting expression is referred to as the *Kohn-Sham decomposition* of the total energy of many-electron systems, and looks like

$$E[n(\mathbf{r})] = T_0[n(\mathbf{r})] + E_{\text{ext}}[n(\mathbf{r})] + E_{\text{cc}}[n(\mathbf{r})] + E_{\text{xc}}[n(\mathbf{r})]. \tag{2.14}$$

Here $E_{\text{ext}}[n(\mathbf{r})]$ represents the external potential energy induced by the surrounding nuclei, $E_{\text{cc}}[n(\mathbf{r})]$ is the energy from classic electronic Coulomb interaction and $E_{\text{xc}}[n(\mathbf{r})]$ is the approximate exchange correlation. Starting with the external lattice energy, the energy functional can be written as

$$E_{\text{ext}}[n(\mathbf{r})] = \int n(\mathbf{r}) V_{\text{ions}}(\mathbf{r}) d\mathbf{r} = \int n(\mathbf{r}) \Big(- \sum_n \frac{Z_n}{\mathbf{r} - \boldsymbol{R_I}} \Big) \mathrm{d}\mathbf{r}, \tag{2.15}$$

which yields a potential operator of the form

$$V_{\text{ext}}(\mathbf{r}) = - \sum_n \frac{Z_n}{\mathbf{r} - \boldsymbol{R_I}}, \tag{2.16}$$

where Z_n marks the atomic number of each individual lattice ion. Moving on, the classic Coulomb interactions between electrons take the same form as in Eq. 2.10, resulting in the potential operator

$$V_{\text{cc}}[n(\mathbf{r})] = \frac{1}{8\pi\varepsilon_0} \int \frac{n(\mathbf{r'})}{\|\mathbf{r} - \mathbf{r'}\|} \mathrm{d}\mathbf{r'}. \tag{2.17}$$

Lastly, in order to treat the exchange-correlation, an approximate potential $\varepsilon_{\text{xc}}[n(\mathbf{r})]$ is introduced. The need of using an approximation rather than an exact model is due to the complex nature of electronic exchange and correlation, which does not display the same simple relations as classical Coulomb interaction. Nonetheless, $\varepsilon_{\text{xc}}[n(\mathbf{r})]$ can be used to formulate an expression for $E_{\text{xc}}[n(\mathbf{r})]$ according to

$$E_{\text{xc}}[n(\mathbf{r})] = \int n(\mathbf{r}) \varepsilon_{\text{xc}}[n(\mathbf{r})] \mathrm{d}\mathbf{r}, \tag{2.18}$$

where the chosen potential simply is integrated over all probability space. Since all constituent terms now are fully determined, the Kohn-Sham auxiliary system can now be used as an approximate equivalent to the real system when describing its ground state energy.

To summarise, by using the expressions from Eq. 2.16 and Eq. 2.17, together with the chosen functional for exchange-correlation $\varepsilon_{\text{xc}}[n(\mathbf{r})]$, Eq. 2.14 can be rewritten in a more useful way. The equation below is denoted the *Kohn-Sham equation*, and takes the form

$$\Big(- \frac{1}{2}\nabla^2 + V_{\text{ext}}(\mathbf{r}) + V_{\text{cc}}[n(\mathbf{r})] + \varepsilon_{\text{xc}}[n(\mathbf{r})] \Big) \psi_i(\mathbf{r}) = \epsilon_i \psi_i(\mathbf{r}), \tag{2.19}$$

which more commonly is recognised as the Schrödinger equation for each individual electron. The solutions $\psi_i(\mathbf{r})$ and ϵ_i are called the *Kohn-Sham orbitals* and *Kohn-Sham eigenenergies* respectively. An important note is that these orbitals are completely fictitious and should thus not be treated as real states. However, they still prove useful in describing electronic properties of the system. Finding the exact solutions to the Kohn-Sham equations corresponds to finding the exact electron density of the system, and hence all the information necessary to describe the dynamics of its constituent particles as implied by Hohenberg-Kohn's first theorem. As such, computational evaluation of these equations represents the cornerstone of DFT-simulations.

2.3 Exchange-correlation functionals

The Kohn-Sham approach facilitates construction of a method that computationally investigates the energies and forces acting upon the particles in the system. Actual implementations of DFT-algorithms usually build on a self-consistency loop, initialised by making a first guess of the ground state-electronic density $n_0^{(0)}(\mathbf{r})$. Using this estimate, the effective potential $V_{\text{eff}}(\mathbf{r})$ is evaluated as

$$V_{\text{eff}}(\mathbf{r}) = V_{\text{ext}}(\mathbf{r}) + V_{\text{cc}}[n(\mathbf{r})] + \varepsilon_{\text{xc}}[n(\mathbf{r})], \tag{2.20}$$

applying the expressions for $V_{\text{ext}}(\mathbf{r})$ and $V_{\text{cc}}(\mathbf{r})$ derived in the previous section, along with a well-suited exchange-correlation potential functional. This is in turn used to evaluate the Kohn-Sham equations from Eq. 2.19, solving for the Kohn-Sham orbitals. After obtaining a value for all ψ_i, the actual ground state density $n_0(\mathbf{r})$ is calculated in accordance with Eq. 2.12, and compared to the initial estimate like

$$\|n_0^{(0)}(\mathbf{r}) - n_0(\mathbf{r})\| \overset{?}{<} \delta, \tag{2.21}$$

where δ is some accepted level of error. If the difference lies within this error margin, the density function is accepted and forces and energies in the system can be evaluated. If it is not accepted, a new estimate $n_0^{(1)}(\mathbf{r})$ is made and the algorithm resets. The loop reiterates until convergence is reached, which ensures self-consistency in the method.

As previously demonstrated, this algorithm relies on the Kohn-Sham approach to replace the ground state density of an interactive, high-dimensional system with that of a non-interactive, exactly soluble system. Within the computational framework, information about particle movement is effectively summarised in an approximate functional of the ground state density. Consequently, the performance of DFT-based computations heavily relies on choosing a well-defined functional for the system under investigation. In many cases it is sufficient to use a simple approximate functional for the exchange-correlation $\varepsilon_{\text{xc}}[n(\mathbf{r})]$. However, in some systems this may lead to a failure in predicting localised states such as polarons and STEs. The error is known as the self-interaction error (SIE), and is in general regarded as one of the major shortcomings of Kohn-Sham DFT [20].

In order to accurately model these formations, correctional methods that account for the SIE therefore need to be constructed. One approach is to introduce hybrid functionals, which incorporate both empirical and ab-initio methods when formulating $\varepsilon_{\text{xc}}[n(\mathbf{r})]$. The idea is to complement the approximate functional by adding parts of exactly derived electronic exchange energy, which in turn cancels out the SIE.

2.3.1 Common exchange-correlation models

Electronic exchange is a quantum mechanical effect arising from the Pauli exclusion principle applied to fermions. The antisymmetric properties of the fermionic wave-function cause electrons of the same spin to repel each other, and electrons of opposite spin to attract. Correlation on the other hand is another aspect of many-body dynamics, the origins of which stem from the actual movement of the constituent particles. Whereas exchange is an inherent property of quantum particles, the correlation energy can be described as a result of electrons affecting each other by their mere presence. In other words, the likelihood of finding an electron in a certain region of space can be affected by the movement and arrangement of all other electrons already found in that region.

Due to the complex nature of these two phenomena, exact evaluation of their respective energies proves problematic. In Kohn-Sham theory, both of these contributions are therefore accounted for by adding an approximative functional $E_{\text{xc}}[n(\mathbf{r})]$ to the total energy. Commonly used methods to construct this include the local density approximation (LDA), and the generalised gradient approximation (GGA). LDA builds solely on electronic density, and takes the general form

$$E_{\text{xc}}^{\text{LDA}}[n] = \int n(\mathbf{r})\varepsilon_{\text{xc}}^{\text{HEG}}[n(\mathbf{r})]\mathrm{d}\mathbf{r}, \tag{2.22}$$

where $\varepsilon_{\text{xc}}^{\text{HEG}}[n(\mathbf{r})]\mathrm{d}\mathbf{r}$ is the combined exchange-correlation energy per particle in a homogenous electron gas. GGA expands on the methodology of LDA by introducing gradients to adjust for the non-homogenous nature of the true electron density. The resulting energy is calculated as

$$E_{\text{xc}}^{\text{GGA}}[n] = \int n(\mathbf{r})\varepsilon_{\text{xc}}^{\text{GGA}}\big[n(\mathbf{r}), \nabla n(\mathbf{r})\big]\mathrm{d}\mathbf{r}, \tag{2.23}$$

which thus includes a way of compensating for density variances in the coordinate surroundings. Evaluating either one of the integrals in the equations above yields an approximation for the total energy contributions of effects related to the exchange and correlation. Moreover, once obtained, the result can in general be separated into its respective components, $E_{\text{xc}} = E_{\text{x}} + E_{\text{c}}$. This is important, since it implies that both LDA and GGA can be linearly combined with other functionals, which in turn provides the basis for hybrid functional methods.

2.3.2 The self-interaction error

In the Kohn-Sham decomposition of the total energy from Eq. 2.14, the classic Coulomb energy functional is formulated as

$$E_{\text{cc}}[n(\mathbf{r})] = \frac{1}{8\pi\varepsilon_0}\int\int \frac{n(\mathbf{r})n(\mathbf{r'})}{\|\mathbf{r}-\mathbf{r'}\|}\mathrm{d}\mathbf{r}\mathrm{d}\mathbf{r'}, \tag{2.24}$$

where $\mathbf{r}$ and $\mathbf{r'}$ mark two points in density space. Due to $E_{\text{cc}}[n(\mathbf{r})]$ being a functional of the electron density, the many-particle electrostatic potential $V_{\text{cc}}[n(\mathbf{r})]$ also becomes a functional of the electron density, as seen in Eq. 2.17. This is a result of reducing the dimensionality of the problem, which of course lowers the computational cost considerably. However, the method involves replacing separate Coulomb interactions with a classical mean field charge distribution, combining the contributions from each individual electron in a single potential. Consequently, when evaluating $E_{\text{cc}}[n(\mathbf{r})]$ as in Eq. 2.24 above, the result is effectively an expression for Coulomb energy where every electron interacts with all of the electrons present in the system, including itself. This spurious interaction is partially corrected by the exchange–correlation functional, but in most cases, especially for localised states, not completely. As such, the formula yields an unphysical contribution to the total Coulomb energy, resulting in the aforementioned SIE.

To increase problems even further, the mean field approximation not only impairs the evaluation of Coulomb energy, but all energies which are derived from electron-electron interactions. This includes the exchange and correlation effects described in section 2.3.1, although their contributions to the total energy typically are much smaller than the Coulomb interaction. Nonetheless, the overall problem of unphysical self-interaction components is embedded into the methodology of Kohn-Sham DFT. As previously stated, this creates problems when trying to describe localised states, and thus calls upon the need for adding correctional terms to the exchange-correlation functional.

2.3.3 Hybrid functionals

Although it remains impossible to exactly evaluate the effects of electronic correlation, there are ways of constructing analytical expressions for electronic exchange. The Hartree-Fock method is an ab-initio model of electronic systems that builds upon similar ideas as the Kohn-Sham approach. However, unlike Kohn-Sham, Hartree-Fock theory includes an exact expression for the exchange energy. Defining the exchange operator as $\hat{K}(\mathbf{r})$, the energy functional takes the form

$$\hat{K}(\mathbf{r})\psi(\mathbf{r}) = \sum_i \phi_i(\mathbf{r})\int \frac{\phi_i^*(\mathbf{r'})\psi^*(\mathbf{r'})}{\|\mathbf{r}-\mathbf{r'}\|}\mathrm{d}\mathbf{r'}, \tag{2.25}$$

where, $\psi(\mathbf{r})$ is the single-electron wave function acted upon by the operator, and $\phi_i(\mathbf{r})$ is the single-electron wave function of another electron indexed i. By including the energy linked to this expression in the final formulation of the total energy

of the whole system, the Hartree-Fock approach fully accounts for electronic exchange within the single-determinant framework, leaving correlation energy as the only discrepancy between the actual system and the auxiliary one.

In hybrid functional DFT, the exact exchange from Hartree-Fock theory is used to balance out the effects of the SIE. By adding a well-defined fraction of the exact exchange energy to the approximative models from section 2.3.1, the self-interacting components can be eliminated. The method is enabled by the generalised Koopmans' theorem, which builds on the piecewise linearity of the total energy with respect to fractional electron number, allowing orbital energies to be interpreted as energy derivatives with respect to occupation. Since self-interaction arises from the effects of individual electrons, a condition can thus be constructed by comparing the energy of a free electron to the energy of an electron within an interacting system. For polarons, this so called Koopmans' condition can be formulated by stating that the single-particle energy of an occupied polaronic state should be equal to the energy of that same state while it looses its occupation [21]. Constructing a hybrid functional thus involves tuning the relevant parameters in order to satisfy this quality, after which self-interaction is eliminated from the system.

One way of generating a hybrid functional is to construct a linear combination of the exact and approximate exchange energies according to

$$E_{\mathrm{xc}} = \alpha E_{\mathrm{x}}^{\mathrm{HF}} + (1-\alpha) E_{\mathrm{x}}^{\mathrm{KS}} + E_{\mathrm{c}}^{\mathrm{KS}}. \tag{2.26}$$

In the expression above, $E_{\mathrm{x}}^{\mathrm{HF}}$ is the exact exchange from Hartree-Fock theory, while $E_{\mathrm{x}}^{\mathrm{KS}}$ and $E_{\mathrm{c}}^{\mathrm{KS}}$ mark the two approximate Kohn-Sham energies. This specific functional is referred to as the PBE0 functional, first presented by Perdew *et al*. [22]. The value of α has to be optimised for the specific material in order to fully cancel out self-interactive effects. This is done by satisfying Koopmans' condition as described above. By doing so, the self-interacting components are cancelled out, and numerical investigations of localised states are enabled. Other hybrid functionals can be constructed as well, but for the scope of this project it is enough to establish PBE0.

3
Method

Since the aim of this thesis is to analyse STEs using hybrid functional DFT, the method is heavily dominated by running extensive simulations on a high-performance computing (HPC) cluster. Obtaining conclusive results largely depends on setting up a working computational framework, as well as designing numerical experiments that yield valuable information about STE characteristics. The outline of this project can be summarised in a few chronological steps, which thus constitute the overall method. Initially, the types of STEs present in the material must be classified to facilitate further investigation. After that, it is possible to study their formation and stability more extensively. Lastly, the analysis can be extended by introducing different surfaces and seeing how these affect charge localisation.

3.1 Cell selection

$BiVO_4$ is a crystalline semiconductor with a variety of possible phases and different surface terminations. Before starting any calculations, the specific configuration thus needs to be specified. The bulk structure with lattice parameters $\{a = b = 10.311, c = 23.594\}$ and properties sampled at $295\,\mathrm{K}$ was chosen as a base sample for this project. This was then cut in different ways to generate two distinguished surface terminations. The original data was first reported by Sleight *et al*, [23], who determined the tetragonal scheelite structure of the crystal. A visualisation of the basic crystalline arrangement is found in Fig. 3.1.

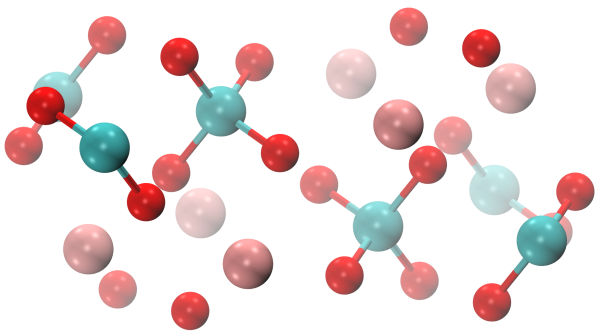

Figure 3.1: The original structure used as a base for reconstructing larger cells, as viewed from a slight angle. Bi atoms are represented by pink spheres, while V and O are marked as blue and red spheres respectively.

Firstly, the structure was cut along the (010)-plane, which generated a flat termination. Two-dimensional layers of VO_4 units and Bi atoms were arranged along the normal axis of the surface, and the two components alternated in a simple periodic fashion, see Fig. 3.2a for details. This profile will henceforth be referred to as the (010)-surface, when speaking specifically about termination characteristics.

The second profile subjected to investigation was generated by cutting the base structure along the (011)-plane, resulting in an uneven termination. This meant that in contrast to the previous configuration, where VO_4 units and Bi atoms were aligned in two dimensional planes, the two components here arranged themselves in a zig-zag pattern relative to the surface, see Fig. 3.2b. This will be referred to as the (011)-surface in conjunction with the first profile. The purpose of using this kind of structure in addition to the previous one was to see how different surface textures may affect charge localisation near the boundaries of the material.

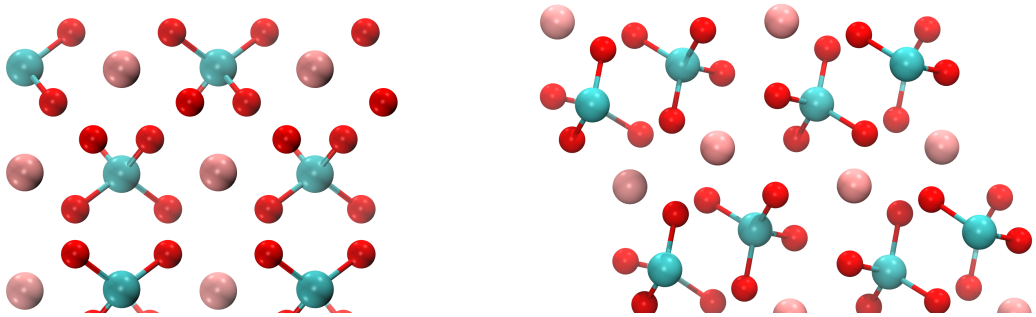

(a) **(b)**

Figure 3.2: Illustration of the two surface samples used during the simulations, highlighting their different arrangement near the termination. The vacuum interface is oriented at the top of each image. The bulks of both samples are geometrically equivalent to each other, as the surfaces essentially are generated by cutting the base cell along different planes. (a) Termination profile of the (010)-sample. One can clearly see that the surface is organised in flat, even layers against the vacuum at the top of the image, with Bi- and V atoms arranged in an alternating fashion. The placement and orientation of the VO_4 units shift and rotate periodically along these layers as one moves further away from the vacuum interface. (b) Termination profile of the (011)-sample. In contrast to the other sample, the surface is now organised in a zig-zag pattern relative to the vacuum interface. This means that there is no clear, two-dimensional layering structure anymore. Instead, Bi atoms and VO_4 units all locate at different distances from the termination, the closest to which being a layer of Bi atoms.

It is important to remember that the (010)- and the (011)-surfaces only differ in their characteristics at the termination. If viewed as part of a larger bulk arrangement, the two cells are equivalent rotations of the same geometry. Therefore, it should be expected that the main differences between localisations in the two structures will appear near the surface. If generated deeper into the cell, the

localised states should theoretically approach those observed in the bulk of the material. However, it is still unclear how deep the surface effects can reach, which highlights the need for studying various domains in the cells.

3.2 Computational details

The crystal specifications of $BiVO_4$ were imported as a CIF-file from the Crystallography Open Database (COD). By using `Python` scripts, this was converted into coordinate files containing the position of each atom, as well as a cell file containing specific information about cell properties. Generating the coordinates was done using a supercell of dimensions $2 \times 2 \times 2$ to reconstruct the tetragonal scheelite structure described in the previous section. The full scripts are found in appendix A. Calculations were carried out using the `CP2K` code-package, which provides a framework for DFT with LDA and GGA, as well as hybrid functional methods [24, 25]. For this project, the PBE0(α) functional was used throughout all simulations to model the exchange-correlation energy. The value of α was set to 0.14 in order to eliminate the self-interaction error, a choice motivated by previous investigations on similar $BiVO_4$ structures [26]. Brillouin zone sampling was done exclusively around the Γ point.

The cell files and coordinate files were used as input for `CP2K`, and referenced in a specific input file passed on to the program. In addition to structural information, this file also contained specifications of all computational variables needed to perform the calculations. This included the specific pseudopotential and basis set used for evaluations, GTH-PBE and ZVP-MOLOPT-SR-GTH respectively. The full copy of one input file is found in appendix B. Simulations were initialised by submitting the input to `CP2K` and declaring the number of nodes to be used on the HPC-cluster, as well defining central processing unit (CPU)-allocation and the number of tasks carried out by each node. After initialising the program, the displacement of each atom towards energy minimum was computed in an iterative process until convergence was reached, signifying that the structure had been relaxed to a stable state. Depending on how the variables in the input file were specified, the relaxed state would either be a triplet, marking the excited state, or a singlet, marking the ground state. The ground state here denotes the absence of free charge carriers in the material, while the excited state refers to electrons and holes being present in the conduction and valence bands, respectively. As such, the samples in this project were always relaxed in their triplet state in order to study charge localisation, except in the cases where ground state energy was specifically sought as a point of reference. If the time limit was reached before all convergence criteria were met, the calculations were restarted from the latest step in the process.

Prior to each STE-simulation, the coordinate files were modified in `VMD` to generate desired outcomes. In order to induce charge localisation, the structure was deformed by moving specific atoms in the cell, lengthening certain bonds and shortening other ones. The reason for this was to perturb the system in such a way that it would favour self-trapping and relax into states of lower energy

than the non-perturbed cell. Since the relaxed state in these cases was specified to a triplet, the existence of lower-energy constellations would mark the presence of localised states within the band gap of the material. Hence, by studying the charge distribution of the perturbed $BiVO_4$-structures after relaxation, the nature and placement of potential STEs could be identified. The exact ways in which the cells were modified differed between each experiment, and a more detailed account for the various methods is presented together with the results in the next chapter. For the ground state simulations, the coordinate files were kept unaltered and simply relaxed in a singlet state.

3.3 Simulations

A number of different simulations were carried out on both surfaces. Initially though, a bulk cell was analysed in order to test the computational setup and verify the configuration against previous results. The cell size was set to 192 atoms. Periodic boundary conditions were applied on all sides of the structure in order to mimic bulk properties.

Moving on, simulations were carried out on the (010)-surface, the size of which also was set to 192 atoms. In order to model surface effects, the cell was extended to contain a region of vacuum on one side, while keeping periodic boundary conditions everywhere else. The vacuum was set to approximately equal length as the cell thickness. After carrying out initial simulations to investigate which STE-formations seemed most likely to appear, calculations were extended to target specific STE-formations. Each outcome was documented and the formation energies for the different charge localisations were compared.

Simulations were then performed on the (011)-surface, which had the same size as the other two cells. Vacuum was also added on one side in the same manner as before. As with the (010)-sample, initial tests were first carried out to see which STEs were most likely to form. Then, specific formations were targeted in order to compare the two surfaces more directly. The exact localisations found in each sample are presented in the following chapter.

Lastly, in addition to performing qualitative tests on the shape and formation of STEs, a set of convergence tests was also done to investigate the effects of dipole-dipole interactions between periodic images and of the k-point convergence. As periodic boundary conditions are imposed on a cell of finite size, dipoles in the neighbouring cells can interact with the ones in the central cell, generating periodic potentials which are not present in the actual bulk system. One way to completely eliminate the effects of these spurious interactions would be to simulate a cell of infinite size, which obviously cannot be done. However, the influence of these unphysical contributions can still be examined by simulating cells of various sizes and extrapolating the results.

New versions of the (010)-surface were therefore generated in order to test the computational convergence in relation to cell size. These new cells consisted of 96 and 648 atoms respectively, and vacuum was added in a way that accounted for their varying thicknesses. Some of the STEs previously observed in the 192-atom

sample were recreated in order to compare their formation energies between the three cells. The convergence test is presented further in chapter 5.

3.4 Result analysis

After the simulations were completed, charge isosurfaces for the states corresponding to the hole and the electron within the STE could be plotted together with the relaxed lattice structure in VMD. The isosurfaces chosen to visualise the results were the densities of each charge carrier. Their corresponding values were set to approximately half of their respective maxima. By studying the shape and formation of the isosurfaces in the relaxed structure, STEs and other localised states could be identified. From the visual results, the STEs were categorised as either *collapsed* or *separated*, based on the previous work described in section 2.1.2. The first of these was characterised by both the hole and the electron localising on the same VO_4 unit. The second category instead saw the electron centre around a VO_4 unit, while the hole localised around a Bi atom. See Fig. 3.3 for details about these different formations. Moreover, the STEs were also classified in different groups depending on where they localised in the cell. This distinction was made for the surface layer, subsurface layer and any of the deeper layers.

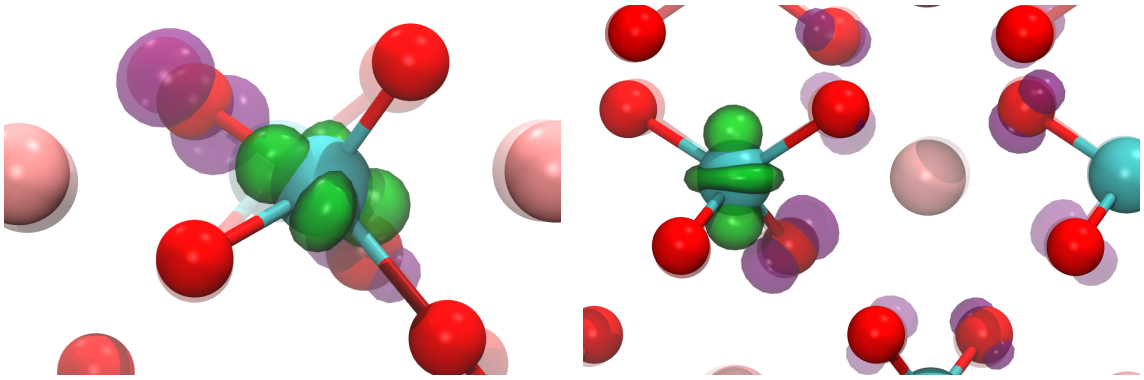

(a) **(b)**

Figure 3.3: Illustration of the two main categories of STEs. Electron density isosurfaces are green, while hole density isosurface are purple. (a) A collapsed STE. Both isodensities are on the same VO_4 unit. The electron concentrates around the V atom, while the hole localises on one or two of the surrounding oxygen atoms. (b) A separated STE. The electron still concentrates around a V atom, but the hole spreads out between multiple oxygen atoms to centre around a neighbouring Bi.

A point worth noting is that the exact shape of the charge isosurfaces usually differed between different types of STEs, as can be seen by comparing Fig. 3.3a and Fig. 3.3b. For instance, electron polarons in separated STEs often displayed isosurfaces resembling the d_{z^2} orbital, while the ones in collapsed STEs exhibited other formations. The main objective of this project is to find and identify STEs

present at the surface of $BiVO_4$, and as such, the exact electron structure leading to their formation is not analysed further here. Nonetheless, the shape and placement of the isodensity surfaces will prove a point of discussion when comparing STEs between the two different surfaces.

In addition to visual classification of the STEs, an analysis was also made with regards to their stability. The formation energy of each result was thus calculated in accordance with Eq. 2.2. From the `CP2K` output file, the total energies of the relaxed structures could be obtained in atomic units. By making ground state simulations for each cell, the corresponding ground state energies could be retrieved in the same way. Furthermore, the band gap of the $BiVO_4$-structure was also collected in eV by making a ground state simulation of the pristine bulk. Introducing a conversion factor of 27.211 between atomic units and eV, the formation energies were thus calculated as

$$E_\mathrm{f} = \left(E_\text{excited state} - E_\text{ground state}\right) \cdot 27.211 - E^\text{CBM-VBM}_\text{ground state}, \tag{3.1}$$

where $E_\text{excited state}$ is the total energy of the excited state and $E_\text{ground state}$ is the total energy of the ground state, both given in atomic units, while $E^\text{CBM-VBM}_\text{ground state}$ is the band gap of the pristine bulk cell, given in eV. Studying the formation energies, the different classes of STEs could be compared and characterised in terms of their stability.

4

Simulation outcomes

This chapter presents the results of all simulations done on the different $BiVO_4$ samples. First, the initial tests on the bulk are compared to those of previous studies to ascertain validity and establish the main points of analysis. Following that, the different localised states found on the (010)-surface are presented. For each of these, an image from one simulation was chosen to represent the results, even though the formation may have appeared in numerous simulations. The results are also discussed briefly to relate them to previous findings and draw conclusions based on the different outcomes. Finally, the experiments made on the (011)-sample are demonstrated in the same manner as the ones made on the (010) one. In addition to presenting the visual and numerical results, a short summary of each method of deformation is also put forward to clarify how lattice deformation was induced.

4.1 Initial bulk tests

As mentioned above, the two simulations performed on the bulk cell were done in order to check the obtained formation energies against previous findings. The cell was deformed by choosing a VO_4 unit in the middle of the structure and lengthening the V–O bonds by varying amounts. In both cases, the simulations resulted in a separated STE. Calculating the formation energies according to Eq. 3.1, these were found to be $-0.83\,\mathrm{eV}$ and $-0.82\,\mathrm{eV}$ respectively. In the previous work done by the group, formation energies around $-0.88\,\mathrm{eV}$ were calculated for separated STEs in the bulk of $BiVO_4$, which corresponds rather well with the values found here. The STE is visualised in Fig 4.1. Green colour is used to illustrate the electron isodensity, while purple is used for the isodensity of the hole. This convention is used for all figures throughout the report.

By studying the visual results, one can see that the electron isodensity forms a combined d_{z^2}-shape around the V atom in the modified VO_4 unit, just like in Fig. 3.3b. The hole on the other hand is dispersed among a multitude of oxygen atoms, all surrounding one of the closest neighbouring Bi atoms, which thus confirms the separated nature of the localisation.

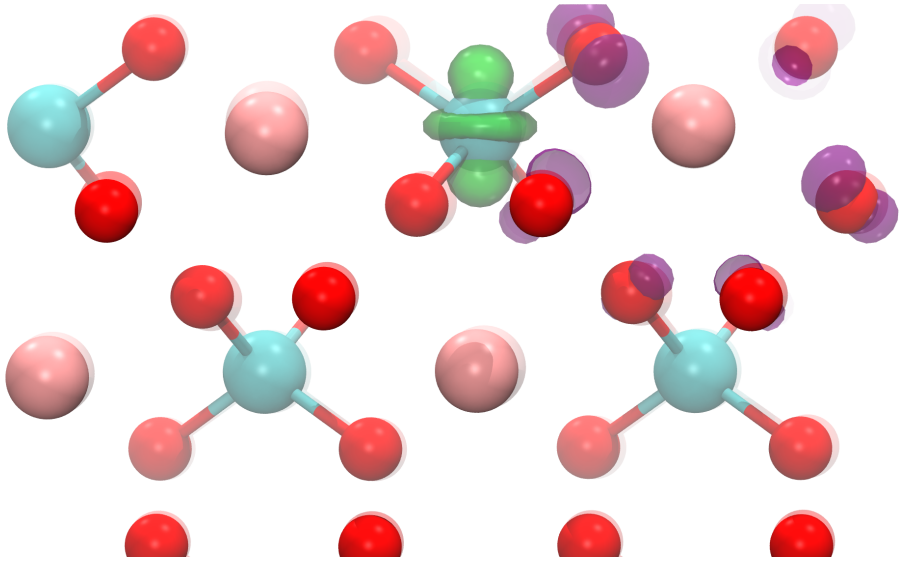

Figure 4.1: Result of the simulations in the bulk. A clearly separated STE can be seen forming between a VO_4 unit and one of the closest neighbouring Bi atoms. The electron isodensity takes on a combined toroidal-dumbbell shape around the V atom, resembling d_{z^2} orbital. The formation energies were calculated to $-0.82\,\mathrm{eV}$ and $-0.83\,\mathrm{eV}$.

To summarise the analysis of the visual representation, the two STEs found in the bulk were both separated, as can be inferred by the shape and placement of the charges in the figure above. In the coming surface tests, separated STEs can thus be compared to the ones found here in order to analyse the differences between the two regions. Collapsed STEs, although not observed in these bulk experiments, display different localisation traits which will be studied more further on.

4.2 Vacuum interface of the (010)-surface

As previously stated, the surface simulations were conducted by extending the cell to contain a slab of vacuum on one side of the cell, effectively generating two vacuum interfaces due to periodic boundaries. In the following section, the results of the experiments on the (010)-surface are displayed and briefly discussed. The STEs are presented in order of types and layers, where the layers are relative to the termination. The *surface* thus denotes the direct vacuum interface, the *subsurface* denotes the layer behind, and the *deep layers* simply denote any of the other layers further in. Visualisations are made so that the vacuum is oriented at the top of the image, while the STE is viewed from one of the sides.

4.2.1 Collapsed STE at surface

As a first step, the vacuum interface was investigated by inducing localisation on one of the VO_4 units in the surface layer in various ways. This was done by

incrementing the length of the V–O bonds little by little, as well as choosing two specific V–O bonds and making them longer than the other two. All of the STEs found in the direct vacuum interface were collapsed, with both the hole and the electron localising on the modified VO_4 unit. In total, 4 instances of this constellation were found. Three of these had formation energies of $-1.04\,\mathrm{eV}$, while one was found to be $-1.06\,\mathrm{eV}$. The visualised structure is found in Fig 4.2 below.

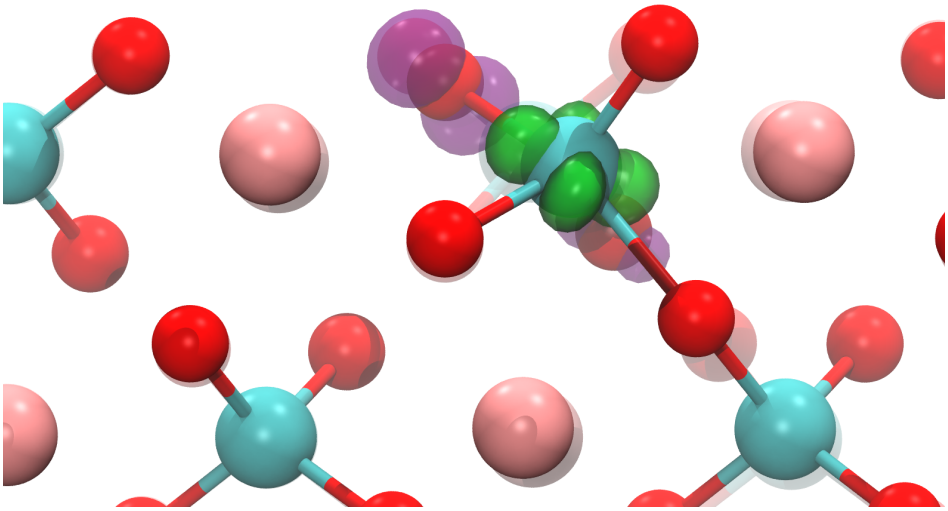

Figure 4.2: The collapsed STE found in the surface of the (010)-sample. The electron isodensity now takes on another shape than the one seen for the separated case. When studying the visualisation, it may appear as if a new bond has been generated between the VO_4 unit in the surface and an O atom further down. However, these "bonds" are only visual representations in VMD, and the extra bond is simply an artifact of certain visualisation settings in the software. In reality, all constituent atoms are bonded in a crystalline lattice structure. The formation energies for this STE were calculated to $-1.04\,\mathrm{eV}$ and $-1.06\,\mathrm{eV}$.

As can be seen in the figure, collapsed STEs display different characteristics from the separated ones. Instead of a d_{z^2} shaped isodensity, the electron showcases four distinct areas of concentration around the vanadium atom. Meanwhile, the hole localises on one or two oxygen atoms in the same VO_4 unit. The fact that most formation energies are about $-1.04\,\mathrm{eV}$ indicates that this formation is very stable, even more so than the separated STEs found in the bulk. Although numerical accuracy still is a subject of further discussion, this observation implies that collapsed STEs are something to be expected in the surface of $BiVO_4$. It also appears that it is quite easy to geometrically achieve this particular localisation, as no other type of STE was found in the direct vacuum interface.

4.2.2 Separated STE at subsurface

The subsurface layer was investigated much in the same way as the surface layer. Initially, a VO_4 unit in the subsurface was modified by lengthening the V–O bonds

by varying degrees. The angles of some of the bonds were also changed in an attempt to generate different outcomes. However, all of the initial tests resulted in separated STEs located around the deformed VO_4 unit, as seen in Fig. 4.3. Additionally, another experiment which was originally meant to analyse the deeper layers, also resulted in a separated STE at the subsurface. As such, this specific formation appeared a total of five times, with the formation energy calculated to $-0.96\,\mathrm{eV}$ for two of them, and $-0.97\,\mathrm{eV}$ for the rest.

The separated STE in the subsurface of the (010)-sample displayed a very similar structure to the ones found in the bulk, with separation occurring between VO_4 units and Bi atoms in the same layer, and the electron isodensity taking the shape of a d_{z^2} orbital. However, just like the collapsed STE found in the surface, this also appears more stable than the bulk formations, albeit by not as much. As such, one seemingly apparent conclusion to draw is that the formation of STEs is altogether more favourable the closer to the surface they are. Although this will have to be a topic for more in-depth analysis, it nonetheless seems likely that the presence of a vacuum interface positively influences the stability of STEs. One primitive explanation for such behaviour may simply be the lack of lattice structure to one side, resulting in lower deformation energies.

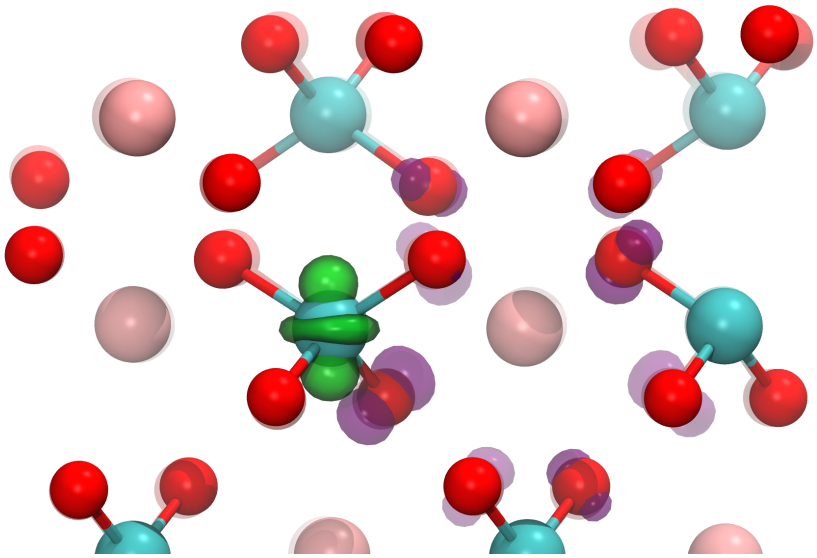

Figure 4.3: A separated STE in the subsurface of the (010)-sample, both the hole and the electron localising one layer behind the direct vacuum interface at the top of the image. The formation energies were $-0.96\,\mathrm{eV}$ and $-0.97\,\mathrm{eV}$.

4.2.3 Collapsed STE at subsurface

Since separated STEs have been observed in the bulk and the subsurface, while collapsed STEs so far only have appeared in the surface, the bulk and the surface regions could potentially constitute two distinct domains where the likelihood of finding each type of STE differs considerably. Making this assumption, the subsurface may theoretically prove a form of middle-ground between them. In order to expand upon this reasoning, a collapsed STE was sought to be created

in the subsurface layer of the cell. This proved more difficult than generating the separated formation, but eventually a collapsed STE could be achieved after testing many different deformations. The formation energy was calculated to $-1.11\,\mathrm{eV}$, which is even more stable than the collapsed STEs in the surface layer.

The formation is visualised in Fig. 4.4. As can be seen, the collapsed subsurface STE has in general the same shape as the one found in the surface. However, one obvious difference lies in the orientation of the electron and hole isodensities. While in the collapsed surface, the hole is located above the electron, here the electron is instead located above the hole. Although the exact reason for this remains undetermined, it could possibly be related to the original orientation of the modified VO_4. The layers in the $BiVO_4$ lattice are essentially organised as periodic iterations of VO_4 units with alternating orientation. If a unit in a certain layer has a specific orientation, the closest units in the immediate sublayer will be of an orientation that exactly mirrors the one above. As such, while the surface VO_4 promotes a collapsed STE where the hole lies closer to the vacuum interface, the subsurface VO_4 will be of opposite orientation, promoting a collapsed STE where the hole lies further away from it.

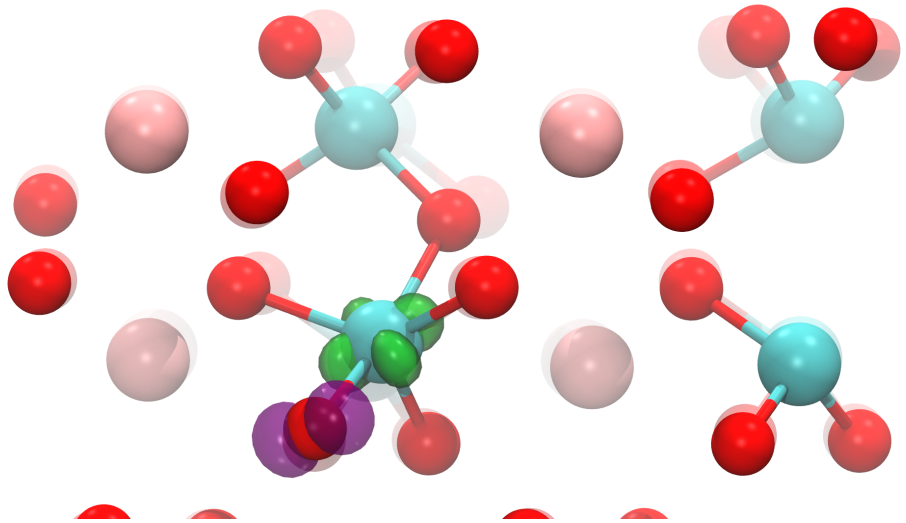

Figure 4.4: The single collapsed STE that was successfully generated in the subsurface. In contrast to the previous collapsed STE found in the surface layer, the hole now localises below the electron, something probably related to the orientation of the VO_4 unit. The formation energy was calculated to $-1.11\,\mathrm{eV}$.

Another interesting point of discussion is the formation energy of this constellation. Despite proving to be geometrically difficult to construct, the collapsed STE in the subsurface appears to be the most stable formation yet, having a slightly lower formation energy than the collapsed STE in the surface. This highlights the difference between energetic and geometric constraints, as the most commonly occurring formations not necessarily are the most stable ones.

4.2.4 Separated STE between layers

In addition to the regular STEs shown in the previous sections, another type of localisation was also investigated. Since separated STEs appear to form almost exclusively within a single layer, an attempt was made to divide up the separation between the surface and the other layers further in. In order to localise the hole polaron in the surface layer, one of the Bi atoms in the near-vacuum vicinity was chosen as anchoring point. The six nearest O atoms were then identified and moved closer to the Bi atom. Meanwhile, a VO_4 unit deeper into the cell was also deformed by modifying the V–O bonds by varying lengths. The location of the VO_4 unit was alternated between the subsurface, the layer behind the subsurface, as well as one of the deeper layers. This resulted in three instances where the hole polaron stayed at the vacuum interface as intended, while the electron localised at the VO_4 unit in the subsurface closest to the anchoring Bi atom. See Fig. 4.5 for details. Moreover, when choosing to modify the VO_4 unit behind the subsurface, a similar result was achieved. The hole polaron still localised around the Bi at the vacuum interface, but now the electron polaron also stayed at the deformed VO_4 atom. As a result, the two charges were separated not only over two layers, but over three layers, see Fig. 4.6. For the first case, all of the formation energies were calculated to $-1.05\,\mathrm{eV}$. This formation thus appears very stable and is comparable to the collapsed STE in the surface terms of formation energy. In the case where separation occurred over three layers, the formation energy was found to be $-0.85\,\mathrm{eV}$. Although this indicates a stable localisation, in absolute terms it is still the lowest value encountered among the STEs explored so far.

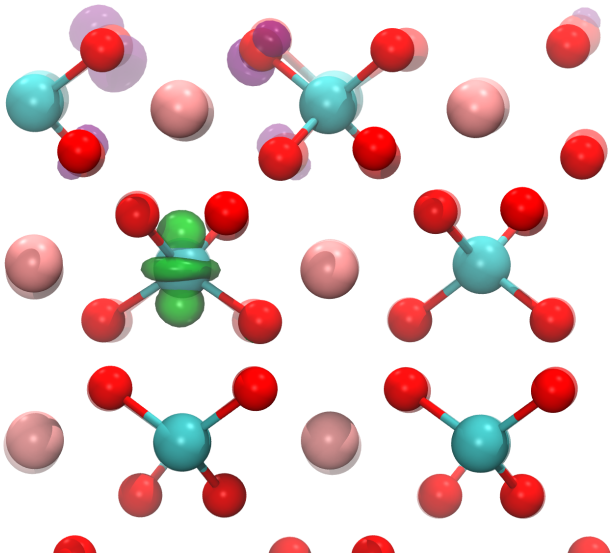

Figure 4.5: One of the new formations where the charges were split up between two different layers. The hole centres around a Bi atom in the surface, while the electron focuses around a VO_4 unit in the subsurface. The electron isodensity still retains the traditional shape of a separated STE, implying that this could be interpreted as a special case where the hole allocates at Bi atom second closest to the VO_4 instead of the closest one. The formation energies were $-1.05\,\mathrm{eV}$.

Studying Fig. 4.5, the isodensity of the electron polaron suggests that this can be seen as a variation of a separated STE, where the hole localises around the second closest Bi atom instead of the closest one. The possibility of forming STEs in this manner could therefore help to explain the apparent difficulty in creating regular separated STEs in the surface layer. As the presence of a vacuum interface somehow obstructs the localisation of two charge carriers at the surface, it may be favourable for one of the carriers to move inwards and instead localise in a layer below. This is supported by the notable formation energy recorded for this specific localisation. Since both collapsed STEs in the surface and the ones displayed in Fig. 4.5 have demonstrated formation energies around $-1.05\,\mathrm{eV}$, the lattice is perhaps more likely to relax into one of these formations than letting both the hole and the electron stay in the surface layer.

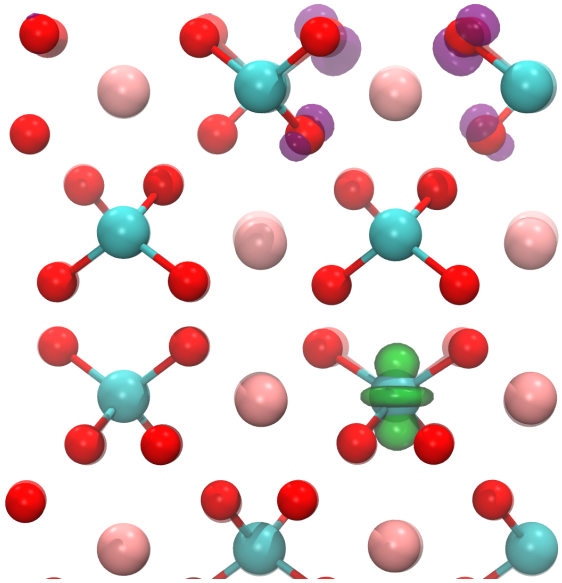

Figure 4.6: The second formation where the hole and the electron split up between layers. This time, the electron localised in the third layer from the vacuum interface, while the hole once again stayed at the surface. The formation occurred once, with a formation energy calculated to $-0.85\,\mathrm{eV}$.

In the case where separation occurs with an additional layer between the two charges, the electron isodensity still retains the characteristic shape of a separated STE, as can be seen in Fig. 4.6. Hence, it should still be appropriate to denote this formation as separated, although the classification as an STE may not be fully accurate since the two polarons lie further apart. This also seems to somehow affect the formation energy of the localisation, as this kind of separation exhibits a value notably smaller in absolute terms than the previous one. This could potentially be attributed to several factors. Firstly, it may simply be due to the distance between them that the formation energy displays a smaller absolute value. To investigate this further, similar structures would have to be generated in other parts of the cell in order to isolate distance between charges as the single parameter. Secondly, the difference in formation energies may also be linked to the previous

discussion about the effects of the vacuum interface. Since the electron is located further away from the surface, it could face a larger energy barrier when deforming the lattice structure to form a polaron. This concept however also needs to be tested further. Lastly, another aspect worth mentioning is the angle between the Bi atom and the VO_4 unit. It is not clear judging from the pictures above, but the subsurface VO_4 showed in Fig. 4.5 is positioned in an angle behind the Bi atom in the surface, simply due to the inherent structure of the lattice. On the other hand, the sub-subsurface VO_4 showed in Fig. 4.6 is located along the same normal axis as the Bi atom. It is unsure how this would affect the stability of the localised state, but it is nevertheless something to keep in mind when conducting future studies on the material.

4.2.5 Separated STE in deeper layer

Three of the simulations resulted in a separated STE located in one of the deeper layers of the material, see Fig. 4.7. This occurred for varying deformations, including modifying V–O bonds in the near-surface level. Since separated STEs seem relatively easy to construct in the bulk, it is not surprising that this kind of localisation would appear when moving further away from the surface. Furthermore, two of the formation energies were calculated to $-0.85\,\mathrm{eV}$, and the third one to $-0.84\,\mathrm{eV}$, which is very close to the STEs found in the initial bulk test. Based on this, it therefore seems that the effects of the vacuum interface are very shallow for the (010)-surface, only affecting localisations one or two layers down into the material. As usual though, this would need further validation in order to be properly established.

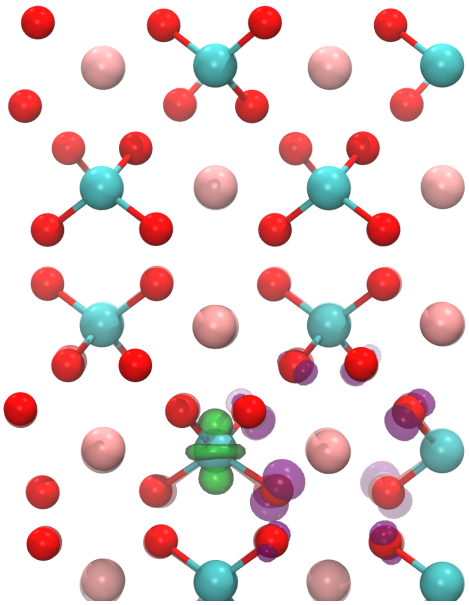

Figure 4.7: A separated STE in the deeper layers of the (010)-sample. This formation appeared three times by modifying VO_4 units in different parts of the cell. The formation energies were calculated to $-0.84\,\mathrm{eV}$ and $-0.85\,\mathrm{eV}$.

An interesting point about these simulations specifically is that for each case, charge localisation appeared at a VO_4 unit separate from the one which was originally modified. This included both VO_4 units in the surface, subsurface and one of the other deep layers. The reason for this apparent movement is most likely a technical issue related to the calculations. Nonetheless, electrons have in previous studies been shown to avoid staying in the direct vacuum interface, highlighting the difficulty in controlling where exactly the charges end up localising. Therefore, it is always important in computational investigations such as this one, to check if one was able to consider all the relevant configurations.

4.3 Vacuum interface of the (011)-surface

The results of the experiments on the (011)-surface are displayed in this section. Initially, the objective was to replicate the same type of STEs as the ones found in the (010)-cell. However, the different characteristics of the (011)-structure instead lead to the detection of many new STEs which were not observed in the previous experiments. Like before, the results are presented with regards to their type and the layer in which they occur. Still, since the geometries here are less obvious, the terminology is explained a bit more in depth. In this case, the *surface* simply denotes the VO_4 units closest to the vacuum interface. Note, however, that in the (011)-structure, there is an additional layer of Bi atoms located slightly above all the topmost VO_4, as can be seen in Fig. 3.2b. These are denoted as the *surface Bi*, in order to distinguish them from the VO_4 surface units, which commonly are the subjects of lattice modification. Furthermore, the *subsurface* here denotes the VO_4 units second closest to the vacuum interface, located near the surface units but in an angle below. Together, the surface and the subsurface mark the zig-zag pattern of VO_4 units which is representative of the (011)-geometry. Any layer below these two is denoted as a *deep* layer.

An important point to remember is that the layering structure is viewed relative to the surface. As mentioned in chapter 3, the (010)- and the (011)-surfaces only differ in the region closest to the vacuum interface, and are equivalent to each other in the bulk. Therefore, when speaking of the uneven layering pattern of the (011)-surface, this is specifically meant to reflect the arrangement of atoms in the near-vacuum vicinity. Like before, the visualisations are oriented so that the vacuum interface is located at the top of the image.

4.3.1 Collapsed STE at surface

First of all, a collapsed STE in the surface layer was sought to be created. This proved surprisingly difficult, as most of the charges instead opted to move deeper into the structure and localise further away from the vacuum interface. Nonetheless, two instances of a collapsed STE could be generated through different modifications. In the first case, the targeted VO_4 unit was moved closer to the vacuum before modifying its V–O bond lengths and relaxing the cell. The resulting STE had a formation energy of $-0.94\,\mathrm{eV}$, and is displayed in Fig. 4.8. In the second

case, localisation was achieved by first modifying a VO_4 unit by lengthening its V–O bonds, followed by identifying the nearest surface Bi and moving the five closest O atoms further away from it. The formation energy was calculated to $-0.90\,\mathrm{eV}$, which corresponds rather well to the first case, although the difference is larger than for any of the other STEs. Visual results indicated that these indeed were the same type of localisation, which suggests that the slight difference in formation energy might stem from the different methods of lattice deformation. The VO_4 unit which was moved further out may have localised a bit closer to the vacuum interface, which thus could lower the energy cost of deforming the lattice.

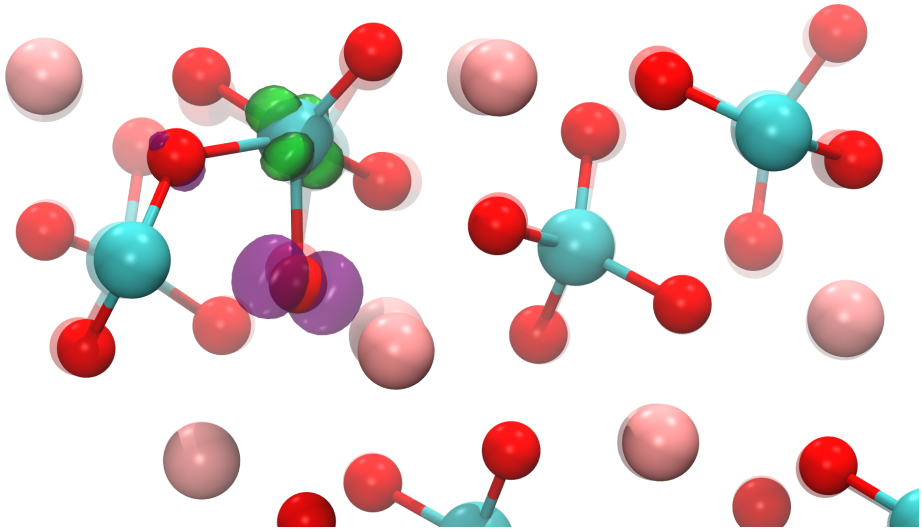

Figure 4.8: The collapsed STE which was observed in the (011)-sample. Once again, the vacuum is at the top of the image. The shape of the isodensities takes on the usual forms of collapsed STEs. Two instances of this formation were generated, with formation energies calculated to $-0.90\,\mathrm{eV}$ and $-0.94\,\mathrm{eV}$.

As seen in Fig. 4.8, both the electron- and the hole isodensity display the characteristic shape of a collapsed STE. The absolute formation energy is not as large as to the one found in the surface of the (010)-structure, which indicates that this STE exhibits a lower overall stability. Following the same theme of discussion as before, this might be a consequence of not being in direct contact with the vacuum. In the (011)-surface, the top-layer of VO_4 can be described as being protected by the above lying surface Bi, which effectively works against lattice deformation. This may also partially describe why the collapsed surface STE seems more difficult to generate in the (011)-surface. Nonetheless, the formation energy is still relatively high in absolute terms, and should technically not provide any hindrance for charge localisation by itself. As such, it may be that the (011)-lattice structure induces the possibility of generating other localisations in the near-vacuum domain, which in turn are more stable or geometrically favourable.

4.3.2 Separated STE at surface

As mentioned in the above section on collapsed STEs in the surface, in many cases the charge carriers moved inwards to localise further away from the vacuum interface. More specifically, though the electron tended to stay on the modified VO_4 unit in the surface, the hole separated and instead centred around a neighbouring Bi atom in the layer below, see Fig. 4.9. Three instances of this localisation were recorded, two of which had a formation energy of $-0.98\,\mathrm{eV}$, while the third was calculated to $-0.97\,\mathrm{eV}$. Although not differing very much from the collapsed STEs in the surface, the different energy levels could still partly explain some of the difficulty in having the electron and the hole staying collapsed on a single VO_4 unit.

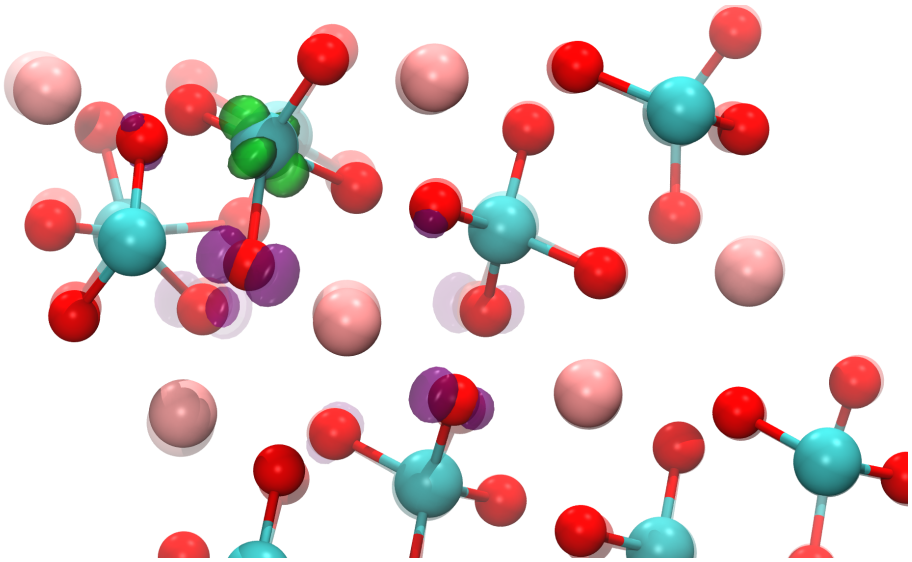

Figure 4.9: The separated STE encountered in the surface layer of the (010)-sample. The hole isodensity takes on its usual shape, displaying distinct separation from the electron and centring around a neighbouring Bi unit. However, two peculiarities stand out in this formation. Firstly, the hole has moved to a Bi atom further down, as there are no VO_4 units and Bi atoms in the same layer. Secondly, the electron isodensity no longer exhibits a d_{z^2} The formation energies were calculated to $-0.97\,\mathrm{eV}$ and $-0.98\,\mathrm{eV}$.

A very interesting point about this separation is that because of the zig-zag pattern of the VO_4 units, the layers are not evenly arranged like the ones in the (010)-surface. The underlying lattice structure may be the same for both samples, but cutting the cell along the (011)-plane generates a skewed termination compared to cutting it along the (010)-plane. As a result, it is impossible for separated STEs to form within a single layer, which is illustrated by the example above. This marks a major difference between the (010)- and the (011)-surfaces, and suggests that separated STEs will have different characteristics depending on the profile of the termination. One such striking example is the shape of the electron isodensity in Fig. 4.9. Although the hole clearly separates from the deformed VO_4 unit, the electron density still has the classic form of a collapsed STE, not displaying the

d_{z^2} shape otherwise seen in separated STEs. It is unclear exactly why this is, but the uneven shape of the lattice might somehow cause different electronic orbitals to be available for excitation. In summary, keeping the zig-zag pattern of the VO_4 units and the unconventional shape of the electron isodensity in mind, the (011)-surface might be able to generate STEs which are unattainable in the structure of the (010)-surface.

4.3.3 Collapsed STE at subsurface

Two types of localisations were encountered in the subsurface of the (011)-sample. The first of these somewhat resembled the collapsed STEs found in the surface layer. When modifying a VO_4 unit in the subsurface, the electron stayed centred at the V atom, while the hole moved to localise on one of the O atoms below. The formation is shown in Fig. 4.10. Three instances of this STE were encountered, for which the formation energies all were calculated to $-1.25\,\mathrm{eV}$. As such, it is the most energetically favourable localisation encountered so far, taking both surfaces into account.

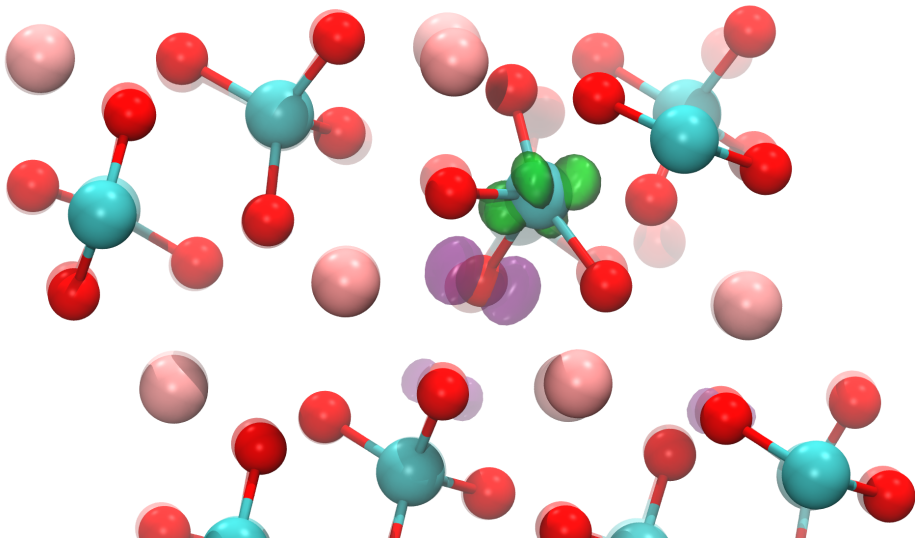

Figure 4.10: The collapsed STE encountered in the subsurface of the (011)-sample. It takes on similar traits as the one found previously in the surface layer. However, although the majority of the hole is found at one of the O atoms in the modified VO_4 unit, small hints of separation can be found in some of the other O units further down. The formation energies of this formation were calculated to $-1.25\,\mathrm{eV}$.

Based on the visual representation above, the STE is regarded as collapsed, supported by the shape and placement of the isodensities. However, apart from the main localisation of the hole on the modified VO_4 unit, a small part of its density can also be seen to locate on some of the electrons further down. Even though the fact that this can be seen at all simply is due to the numerical values chosen to represent the isosurfaces, a small ambiguity like this could potentially hint at

weak traces of separation. Since it is more visible for this formation than for any of the other ones previously studied, it might be an indication of the electron and the hole being slightly further apart than in a normal collapsed STE. Though still just a hypothesis, it could perhaps be linked to the kind of separation seen in the surface layer, where the separated STE exhibited unconventional electronic isodensities. As such, there might prove to be a larger gray area between collapsed and separated STEs in an uneven termination.

4.3.4 Separated STE at subsurface

The other formation detected in the subsurface more resembled a regular separated STE. This was encountered two times when modifying VO_4 units in any of the deeper layers. As this was done, the electrons stayed at the V atom, while the hole moved up to centre around one of the Bi atoms above. Interestingly enough, this was the only case in the (011)-structure where the the hole localised closer to the vacuum interface than the electron, see Fig. 4.11. The formation energies were calculated to $-1.20\,\mathrm{eV}$ for both instances, also proving to be a very stable formation.

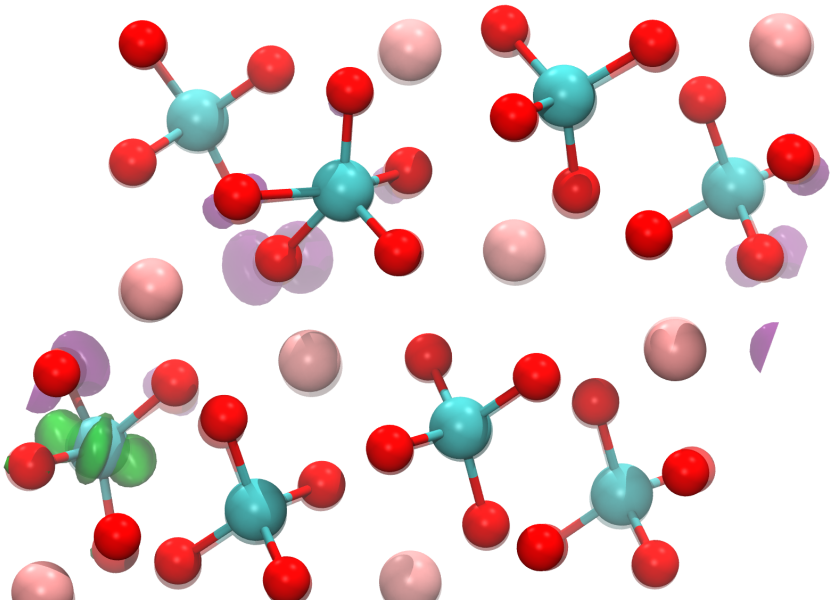

Figure 4.11: The other case found in the subsurface of the (011)-structure. Although the electron is located further down, the STE is regarded as a subsurface formation due to the placement of the hole. Notably, the electron isodensity regains its d_{z^2} shape. The formation energies were calculated to $-1.20\,\mathrm{eV}$.

Looking at the visualised state, it is clear that this resembles a traditional separated STE much more than anything encountered in the (011)-sample so far. For the first time during these experiments, the electron isodensity regained its d_{z^2} shape, which has been characteristic for separated STEs in the bulk and the (010)-sample. Moreover, the hole is clearly divided up between O atoms in the subsurface and the sub-subsurface, centring around one of the lower Bi atoms. Even

though the electron is located in the deeper part of the cell, the STE is here classified as a subsurface-structure due to the placement of the hole. It is unclear why this was not encountered in any of the layers closer to the vacuum interface, both the shape of the electron isodensity and the hole being above the electron. On the other hand, it is not surprising that the regular STE formation is recovered when moving further away from the vacuum interface. As previously established, the bulks of the two samples are equivalent to each other, meaning that the effects of the uneven layering pattern should be most prominent near the surface. Nonetheless, the formation energies are far from those obtained during the bulk simulations, suggesting that one may need to move further into the cell in order to reach the bulk domain of the (011)-sample.

4.3.5 Separated STE in deeper layer

Lastly, another separated STE was also recorded where both the electron and the hole localised in the deeper layers. This only occurred once, after simultaneously modifying a VO_4 unit in the surface and one of the lower Bi atoms. Like the previously discussed separated STE in the subsurface of the (011)-sample, this also resembled the ones found in the bulk more closely than the localisations observed near the vacuum interface. The electron isodensity once again regained the traditional d_{z^2} shape, and the hole centred around the nearest Bi atom, see Fig. 4.12. This is not surprising, given as the deeper layers are closer to the bulk domain. The formation energy was calculated to $-1.05\,\mathrm{eV}$, proving it to be a stable formation, though still less so than some of the ones previously observed.

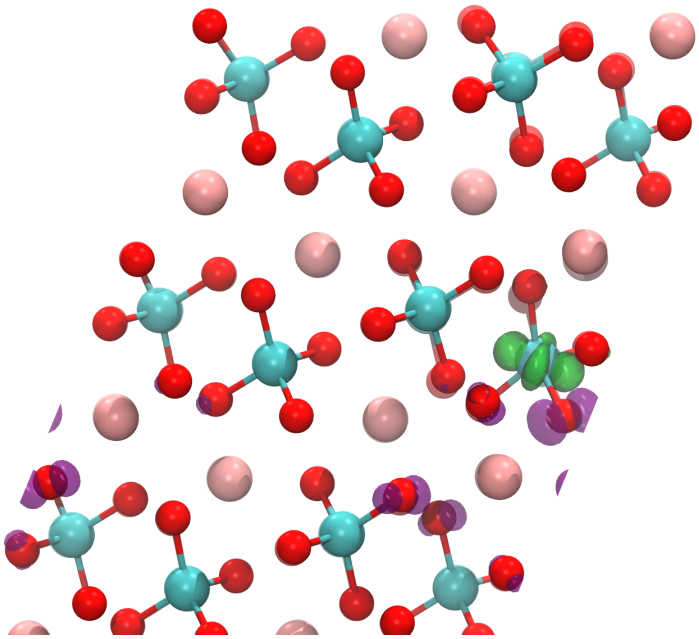

Figure 4.12: The last formation found in the (011)-sample, a separated STE in one of the deeper layers. Comparing it to the separated STE in the subsurface, one can see that they are structurally very similar. This localisation was observed once, and its formation energy was calculated to $-1.05\,\mathrm{eV}$.

Studying the STEs in both Fig. 4.11 and Fig. 4.12, it becomes clear that these two are configuratively equivalent to the separated STEs found in the bulk. The fact that the electron again localises above the hole could be an effect of alternating orientation of the VO_4 units, rather than relating to properties at the surface. The STE in Fig. 4.11 should perhaps be interpreted in the same way, implying that for electrons below the subsurface, the hole simply localises at the closest Bi atom without heeding potential effects of the vacuum interface.

Comparing the formation energies, the separated STE in the deep layer is less stable than the ones in the subsurface, but still notably more stable than the bulk formations. Although the shapes of the deeper localisations thus approach the bulk-STEs as expected, it seems that the bulk domain of the cell has yet to be fully reached. For the (010)-surface, the separated STEs in the deeper layers displayed very similar formation energies as the bulk STEs, implying that the effects of the vacuum interface only reach two or three layers down into the cell. Here however, the surface still seems to influence the stability of localisations found below the sub-subsurface level. This could partially be explained by the inherent structure of the (011)-surface. Due to its specific layering pattern, the layers below the surface and subsurface are closer to the vacuum interface than the corresponding layers in the (010)-surface, meaning that surface effects should be more prevalent. Still, it cannot be completely ruled out that the specific profile of the termination also influences the depth of the surface effects. In the near-vacuum domain it has here been established that different terminations seem to affect localisation properties, but it remains to be seen where exactly the bulk domain starts for various surfaces. In order to test this, a larger (011)-sample would have to be used, as the one used here did not prove deep enough to eliminate surface effects.

5

Results summary and further analysis

As was demonstrated in the previous chapter, a number of different STEs were found both in the (010)- and the (011)-surfaces. This chapter aims to summarise the results and present the formation energies in a more accessible format. The main points of analysis are also brought up again as the two surface structures are compared head to head. The results of the convergence test are also presented, along with a short analysis on its implications for numerical stability.

5.1 Surface comparison

A total of six different localisations were observed in the (010)-surface, while five were found in the (011)-surface. As expected, the main difference between the two structures were observed in the near-vacuum vicinity, where the charge carriers were more exposed to the distinct surface profiles. This was especially true for the shape and type of the STEs which appeared in the various layers, while the formation energies differed more throughout the structure as a whole.

In the (010)-surface, only collapsed STEs were obtained in the direct vacuum interface. The (011)-surface on the other hand showcased both collapsed and separated STEs, demonstrating a broader geometric range of localisation in this domain. However, these separated STEs were of a different character compared to the ones usually found in the bulk, with electronic densities resembling those of traditionally collapsed STEs.

In the subsurface, both structures displayed separated and collapsed STEs, even though only parts of the separated STE localised in the subsurface of the (011)-cell. In this case, the electron centred at a VO_4 unit in one of the deeper layers, signifying a sort of separated STE in the "far end" of the subsurface. The fact that this kind of formation appeared at all was a consequence of the zig-zag pattern of the layers in the (011)-surface. Additionally, the collapsed STEs in this sample potentially also showcased small signs of separation, indicating that the electron and hole polarons may lie further away from each other than in usual collapsed formations.

In the deeper parts of the two cells, localisations were very similar. Both the (010)- and the (011)-structure generated separated STEs, geometrically equivalent to the bulk STEs if viewed with periodic boundaries. Yet, the formation energies differed between them. In the (010)-cell, the values were very similar to those ob-

tained for the bulk formations, suggesting that the effects of the vacuum interface were very shallow in this case. In the (011)-cell on the other hand, the separated STEs in the deeper layers were more stable than the ones found in the bulk, indicating that the vacuum interface still affected formations in some way. This could perhaps result from the deep VO_4 units lying closer to the surface due to the skewed structure of the cell, although the full effects of the termination profile remain to be explored in higher detail.

Lastly, the (010)-structure also displayed two formations where the charges separated between different layers. While the hole centred around a Bi atom in the surface, the electron instead localised on a VO_4 unit one or two layers further down. This opens up interesting possibilities of charge localisation, since separated STEs in the (010)-structure otherwise tended to localise within a single layer relative to the vacuum interface. The formation energies of all the found charge localisations are summarised in Fig. 5.1, illustrating the main differences between the (010)- and the (011)-surfaces.

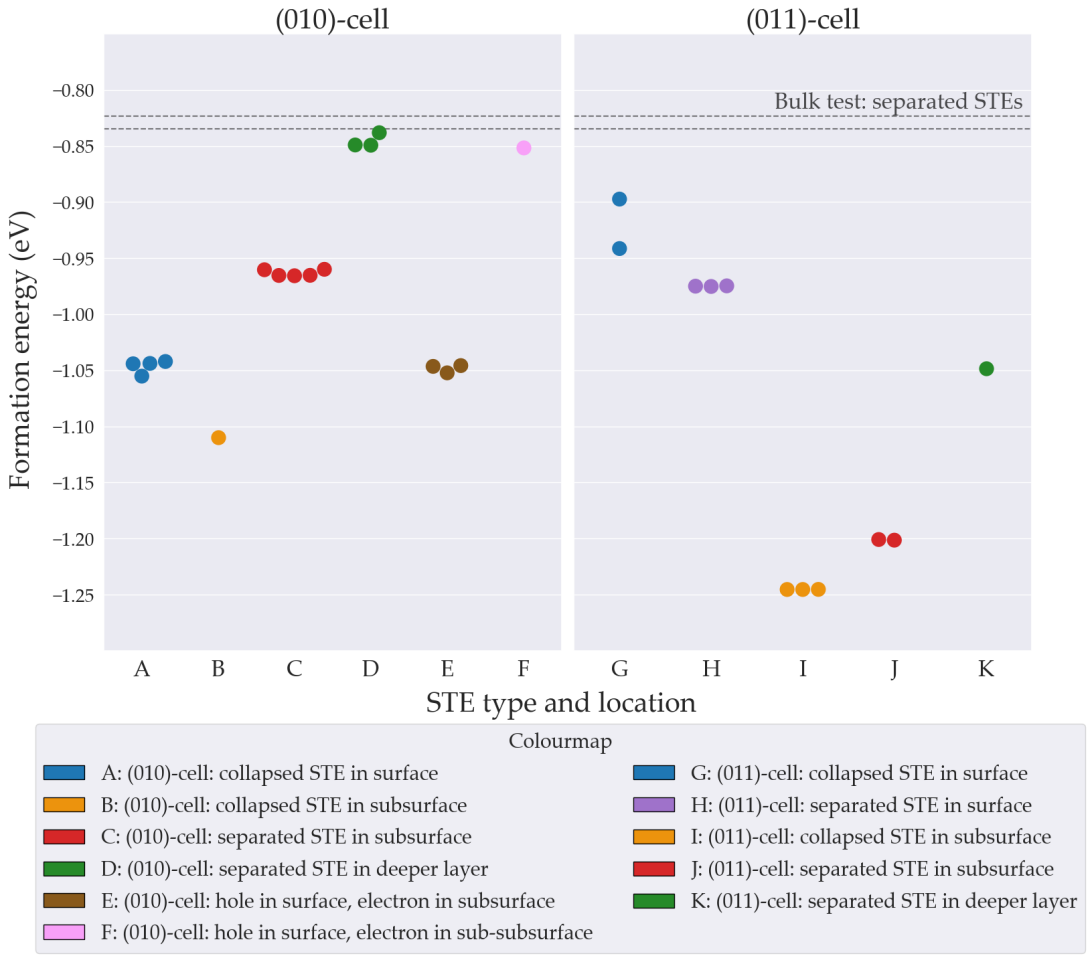

Figure 5.1: A graph displaying the various formation energies of the different STEs. It is hard to make out any general patterns, but the two most stable localisations were both found in the subsurface of the (011)-structure. Moreover, comparing the two structures, the most stable localisation in each case proved to be the collapsed STE in the subsurface.

Studying the figure above, it is hard to draw any definite conclusions other than what kind of localisations are feasible. One main observation however is that the localisations in general seem more stable in the (011)-surface than in the (010)-surface, at least when moving away from the direct vacuum interface. Moreover, it is clear that most of the STEs consistently produced very similar formation energies, apart from the collapsed STE in the surface of the (011)-structure (case G in Fig. 5.1). As mentioned previously, this might be due to the rather different methods of lattice deformation for the two experiments, but it is difficult to say with full certainty.

One of the few things the two surfaces had in common is that the lowest formation energy was encountered for collapsed STEs in the subsurface of the cell. In the (010)-structure, this specific localisation proved somewhat laborious to achieve, but once generated it apparently proved to be very stable. The one in the (011)-structure on the other hand appeared more frequently, and additionally demonstrated even lower formation energies. Why these formations in particular seemed the most stable could be a combination of various factors. Since it is located close to the termination, it might be that the energy cost of deforming the lattice is relatively low. At the same time, being one layer below the direct vacuum interface may imply that the energy potentially gained by doing so is greater than in the surface layer, since there are more atoms in the near vicinity which can contribute to the localisation. As such, the subsurface might be set at an optimal distance from the vacuum interface for stable STE formation, at least in the collapsed case.

Instead studying the separated STEs in the subsurface, the ones found in the (011)-cell (Case J) also proved very stable, having the second lowest formation energy of all formations across both structures. It is important to remember however that only parts of this configuration were located in the subsurface, as the electron localised further down. In contrast, the separated STE in the subsurface of the (010)-cell (case C), where the whole STE was located in the subsurface, the formation energy in absolute terms is considerably smaller. This might potentially be attributed to the different termination profiles of the surfaces, but the exact reason for the discrepancy is unclear.

Now looking at the surface layers of the two structures, at least one other pattern could be discerned. In the (010)-cell, collapsed STEs in the surface (case A) are relatively stable, while both the collapsed and separated STEs in the surface of the (011)-cell (case G and case H) are notably less so. In connection with the results presented in chapter 4, it was speculated that this might be due to the VO_4 units in the (011)-cell being "protected" by another layer of surface Bi, increasing the energy needed to reconstruct the lattice. However, based on the above discussions about the subsurface, this hypothesis can be elaborated further. While the collapsed STEs in the surface of the (010)-cell may be experiencing a lower energy barrier to deform the lattice, though at the same time not gaining as much due to the lack of surrounding bonding atoms, the collapsed STEs in the surface of the (011)-cell may suffer from the double negative effects of their position. In addition to the surface Bi working against lattice deformation, the lack of other neighbours at the top of the (011)-cell might also lead to less energy being gained

in the localisation process. Still, all of this is highly speculative, and a further research would have to be done before any conclusions could be drawn based on these assumptions.

The two cases in the (010)-surface where the hole and the electron separated between different layers also proved to be very distinct from each other. Firstly, when the hole centred around a Bi atom in the first layer and the electron localised in the subsurface (case E), the formation energy was similar to the collapsed STEs found in the surface of the structure. Interestingly enough, they were also more stable than the separated STEs in the second layer. Interpreting this state split up between surface and subsurface as a special variant of a separated STE, one can make the observation that for the (010)-lattice structure, the separated states which are at least partially located at the surface of the material are favoured over separated STEs located further down. As noted before, the opposite is true for the (011)-surface, meaning that there seems to be no clear placement favouring the separated STEs. The second case, where the electron located two layers below the hole (case F), displayed one of the weakest formations seen in these tests, comparable to the energies found in the bulk. It thus appears that separating holes and electrons more than one layer apart will decrease stability rather than increase it.

Lastly, it should also be noted that as the separated STEs move deeper into the lattice, they should approach the lines which represent the initial bulk tests. This pattern can be seen very clearly for the (010)-surface, where the separated STEs in the deeper layers almost perfectly align with the ones in the bulk. In the (011)-surface, the trend also seems to be that the STEs in the deeper layers become more prone to separate and exhibit formation energies that approach the ones of the bulk STEs. However, as discussed previously, the bulk domain was not fully reached for the (011)-surface, requiring larger cells to examine when exactly it is reached for this kind of lattice structure.

5.2 Convergence tests

The convergence tests were carried out in order to examine the effects of spurious dipole-dipole interactions on the calculation of formation energies, and estimate how these would change if the dipole charges were completely isolated. The original cell contained 192 atoms, while the new ones consisted of 96 and 648 atoms respectively. Additionally, another cell of 768 atoms was also meant to be investigated, but the computations on this cell ultimately turned out to be too costly and did not finish in time for the report. It would still be useful to conduct simulations in this cell size in the future. These specific sizes were chosen as 648 corresponds to repeating the 192-atoms cell $1.5\times$ in every direction, while 768 corresponds to repeating the 96-atoms cell $2\times$ in every direction.

The aim was to recreate three of the previously acquired localisations on the new cells, and compute their formation energies in the same manner as before. The three localisations chosen to recreate were a collapsed STE in the surface (case A in Fig. 5.1), a separated STE in the subsurface (case C) and a separation where

the hole localised in the surface and the electron localised in the subsurface (case E). The outcomes of these new simulations are all summarised in Fig. 5.2.

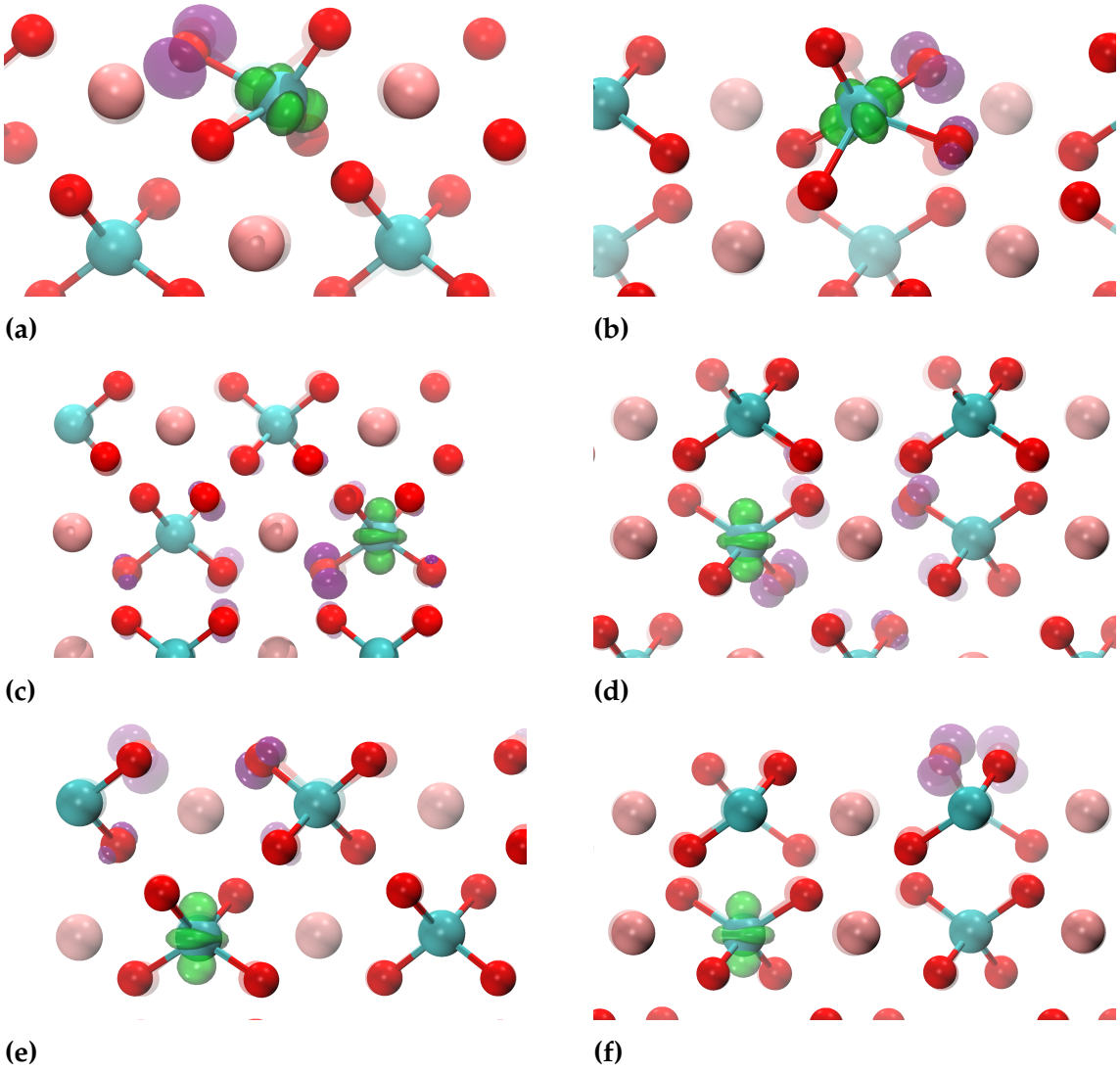

Figure 5.2: The outcomes of the convergence tests. For each formation, the results resembled those previously found in the (010)-surface of 192 atoms, except for the case presented in Fig. 5.2f. There, instead of the hole centring around a Bi atom in the surface, it appears to localise on a VO_4 unit without heeding the Bi. It is unclear exactly why this is, so it was decided to exclude this result from the convergence evaluation. (a) 96 atoms: collapsed STE in surface layer. The formation energy was calculated to $-0.93\,\mathrm{eV}$. (b) 648 atoms: collapsed STE in surface layer. The formation energy was calculated to $-1.12\,\mathrm{eV}$. (c) 96 atoms: separated STE in subsurface layer. The formation energy was calculated to $-0.84\,\mathrm{eV}$. (d) 648 atoms: separated STE in subsurface layer. The formation energy was calculated to $-1.00\,\mathrm{eV}$. (e) 96 atoms: hole in surface, electron in subsurface. The formation energy was calculated to $-0.90\,\mathrm{eV}$. (f) 648 atoms: hole in surface, electron in subsurface. Due to the unusual formation, this result was excluded from the evaluation.

As can be seen in Fig. 5.2, all of the sought localisations were successfully reconstructed in the cell containing 96 atoms. However, for the larger cell of 648 atoms, the last simulation did not generate a localised state corresponding to the same results as the other ones. As such, this was disregarded when comparing the different formation energies, leaving only two points of comparison for the case with hole and electron split up between two different layers.

The final results are found in Fig. 5.3, where the formation energies are plotted as functions of the inverse cell size. This specific representation was chosen in order to extrapolate the results towards zero in an uncomplicated fashion. In the case where the inverse is taken instead of the direct cell size, approaching zero on the x-axis corresponds to approaching a cell of infinite size, and hence also the case with isolated dipoles. Moreover, since all cases resulted in more or less linear behaviour when plotting the results in this way, the extrapolation could be done as a simple linear fit. To represent the formation energies of the original 192-atoms cell, which in some cases had been calculated to more than one value, an average was calculated from the previous results.

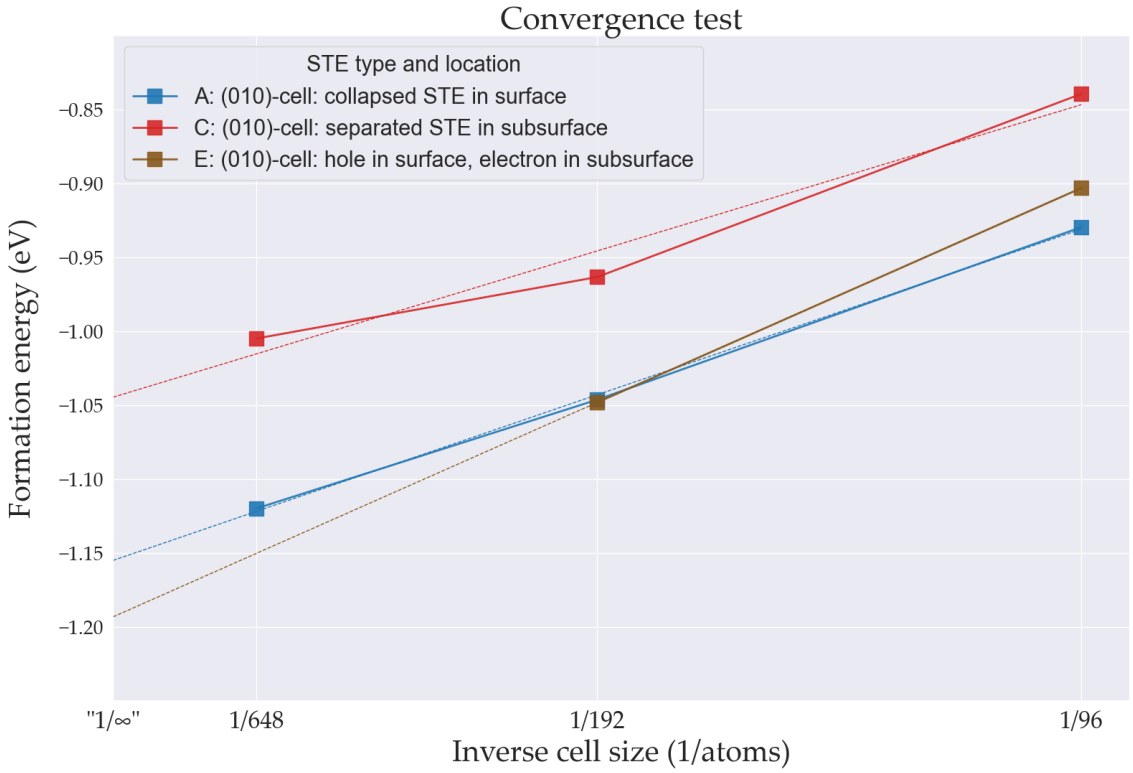

Figure 5.3: The formation energies of cases A, C and E, calculated for different cells. The x-axis denotes the inverse of the cell sizes, meaning that the larger cells are found further to the left in the plot. A linear extrapolation is done towards zero, which in this case is written as "$1/\infty$" to mark the fact that it represents a cell of infinite size. In theory, the points where the linear extrapolations intersect with the y-axis correspond to the actual formation energies of the different cases. That is to say, if the simulations were not affected by dipole-dipole interactions between periodic images.

By looking at the plots in Fig. 5.3, it becomes clear that there is an obvious trend of larger cells generating lower formation energies. This applies uniformly across all cases, and implies that the presence of spurious potentials caused by the interacting dipoles generally leads to an overestimation of the formation energies, making the STEs appear less stable than they actually are. Following the linear extrapolations towards zero, the theoretical formation energies for a cell of infinite size can be read as the value of the intersections with the y-axis, all of which are lower than the previously reported values for the cell of 192 atoms. However, it is still dubious how much weight should be placed on the exact values of these intersections. Although the blue data points form almost a perfect linear line, the red data points demonstrate a hint of potentially more complex behaviour. Meanwhile, the brown data only consists of two points, making the validity of the extrapolation rather debatable. Nevertheless, the most important note to make for this report specifically, is that the formation energies for the different cases seem to follow each other rather well between varying cell sizes, indicating that their relative stability is more trustworthy. That being said, the results are still impaired by the fact that only two data points were obtained for case E, and it would prove well worthwhile to continue this investigation further on.

6
Conclusions and outlook

This project demonstrates the importance of identifying localised states in materials used for next-generation water splitting devices, focusing on the common photoanode $BiVO_4$. Using hybrid functional DFT to simulate charge localisations in an excited lattice configuration, multiple cases of STEs were found in the near-vacuum interface of the material. A simple crystalline structure was first imported to perform initial tests on the material bulk. Then, two surface profiles were generated by cutting the cell along two different planes. Localisation was achieved by modifying certain bonds in the cell and relaxing the lattice structure in a triplet state. By calculating the formation energies of each state, their stabilities could be compared.

It was found that for both a flat- and a skewed surface profile, the most stable formation was a separated STE located in the layer below the direct vacuum interface. This was a rare agreement between the two surfaces, as it appeared that the shape of the termination greatly affected both the type and stability of STEs near the material edge. For an even layering pattern, the formation energies were quite similar between different layers. For an uneven layering pattern however, the STEs found in the subsurface layer were more stable by far than those found in the surface layer, exhibiting the two lowest formation energies found overall. As localisations were moved deeper into the cell, STE-types and formation energies approached those of the initial bulk tests. In the sample with a flat termination, the stability fully converged below the subsurface, indicating that surface effects are quite shallow in this structure. In the sample with a skewed termination, the same pattern could be observed, although the stabilities did not fully converge with the bulk values. It is unclear whether this had more to do with the absolute distance from the vacuum interface, or if this kind of skewed structure proved generally more favourable for STE formation also deeper into the cell.

In the convergence tests it was concluded that the formation energies found in larger cells were lower than those found in a cell of 192 atoms, which here was the main subject of investigation. As such, the localisation should be expected to be even more stable when increasing the number of atoms in the cell. Although the exactness of these actual values remains to be further analysed, this trend was clear to see for all the cases which were tested. Moreover, it still appears like the relative stabilities between the various STEs demonstrated in this report can be trusted.

Finally, although the conclusions presented here will contribute to the understanding of charge localisation in $BiVO_4$, and by extension also its potential use

as a photoanode for water splitting, the surface has only been analysed at a vacuum interface. If the material is to work in real devices, it will of course have to function also in wet environments. To continue this work, new projects should therefore try to incorporate water molecules at the material interface, and see how these influence charge localisation. Water molecules are electric dipoles, and could potentially affect certain aspects of charge dynamics in the surface of the crystal structure. Consequently, it will prove imperative for practical applications to further experiment on $BiVO_4$ in such conditions. Another point of continued investigation would be to include other, more computationally robust packages such as `VASP`, to increase the accuracy of the computations.

Bibliography

[1] Michael Grätzel. Photoelectrochemical cells. *Nature*, 414:338–344, 2001.

[2] Allen J. Bard and Marye Anne Fox. Artificial photosynthesis: Solar splitting of water to hydrogen and oxygen. *Accounts of Chemical Research*, 28(3):141–145, Mar 1995.

[3] Michael G. Walter, Emily L. Warren, James R. McKone, Shannon W. Boettcher, Qixi Mi, Elizabeth A. Santori, and Nathan S. Lewis. Solar water splitting cells. *Chemical Reviews*, 110(11):6446–6473, 2010. PMID: 21062097.

[4] J. K. Norskov, T. Bligaard, J. Rossmeisl, and C. H. Christensen. Towards the computational design of solid catalysts. *Nature Chemistry*, 1(1):37–46, Apr 2009.

[5] Abhishek B., Jayarama A., Arjun Sunil Rao, Sanjog S. Nagarkar, Arnab Dutta, Siddhartha P. Duttagupta, Sriganesh S. Prabhu, and Richard Pinto. Challenges in photocatalytic hydrogen evolution: Importance of photocatalysts and photocatalytic reactors. *International Journal of Hydrogen Energy*, 81:1442–1466, 2024.

[6] Akihiko Kudo, Keiko Omori, and Hideki Kato. A novel aqueous process for preparation of crystal form-controlled and highly crystalline $BiVO_4$ powder from layered vanadates at room temperature and its photocatalytic and photoph ysical properties. *Journal of the American Chemical Society*, 121(49):11459–11467, 1999.

[7] Hongmei Luo, Alex H. Mueller, T. Mark McCleskey, Anthony K. Burrell, Eve Bauer, and Q. X. Jia. Structural and photoelectrochemical properties of $BiVO_4$ thin films. *The Journal of Physical Chemistry C*, 112(15):6099–6102, 2008.

[8] Hosung Seo, Yuan Ping, and Giulia Galli. Role of point defects in enhancing the conductivity of $BiVO_4$. *Chemistry of Materials*, 30(21):7793–7802, 2018.

[9] Ian D. Sharp, Jason K. Cooper, Francesca M. Toma, and R. Buonsanti. Bismuth vanadate as a platform for accelerating discovery and development of complex transition-metal oxide photoanodes. *ACS Energy Letters*, 2(1):139–150, 2017.

[10] Ganesh S. Kamble and Yong-Chien Ling. Solvothermal synthesis of facet-dependent $BiVO_4$ photocatalyst with enhanced visible-light-driven photocatalytic degradation of organic pollutant: assessment of toxicity by zebrafish embryo. *Scientific Reports*, 10(1):12993, Aug 2020.

[11] Aron Walsh, Yanfa Yan, Muhammad N. Huda, Mowafak M. Al-Jassim, and Su-Huai Wei. Band edge electronic structure of $BiVO_4$: Elucidating the role of the Bi s and V d orbitals. *Chemistry of Materials*, 21(3):547–551, 2009.

[12] Jinzhong Zhang, Jueli Shi, Yihong Chen, Kelvin H. L̃. Zhang, and Ye Yang. Bimolecular self-trapped exciton formation in bismuth vanadate. *The Journal of Physical Chemistry Letters*, 13(42):9815–9821, 2022.

[13] Erwin N. Fernandez, Daniel A. Grave, Roel van de Krol, and Fatwa F. Abdi. Strain-induced distortions modulate the optoelectronic properties of epitaxial $BiVO_4$ films. *Advanced Energy Materials*, 13(25):2301075, 2023.

[14] Kyoung E. Kweon, Gyeong S. Hwang, Jinhan Kim, Sungjin Kim, and Seong-Min Kim. Electron small polarons and their transport in bismuth vanadate: a first principles study. *Phys. Chem. Chem. Phys.*, 17:256–260, 2015.

[15] Taifeng Liu, Mengsi Cui, and Michel Dupuis. Hole polaron transport in bismuth vanadate $BiVO_4$ from hybrid density functional theory. *The Journal of Physical Chemistry C*, 124(42):23038–23044, 2020.

[16] Julia Wiktor, Francesco Ambrosio, and Alfredo Pasquarello. Role of polarons in water splitting: The case of $BiVO_4$. *ACS Energy Letters*, 3(7):1693–1697, 2018.

[17] Feng Wu and Yuan Ping. Combining landau–zener theory and kinetic monte carlo sampling for small polaron mobility of doped $BiVO_4$ from first-principles. *J. Mater. Chem. A*, 6:20025–20036, 2018.

[18] Monika Stanke. *Adiabatic, Born-Oppenheimer, and Non-adiabatic Approaches*, pages 1–51. Springer Netherlands, Dordrecht, 2016.

[19] Robert G. Parr and Yang Yang Weitao. *Density-Functional Theory of Atoms and Molecules*. Oxford University Press, Incorporated, Oxford, UNITED STATES, 1994.

[20] Junwei Lucas Bao, Laura Gagliardi, and Donald G. Truhlar. Self-interaction error in density functional theory: An appraisal. *The Journal of Physical Chemistry Letters*, 9(9):2353–2358, May 2018.

[21] Stefano Falletta and Alfredo Pasquarello. Polarons free from many-body self-interaction in density functional theory. *Phys. Rev. B*, 106:125119, Sep 2022.

[22] John P. Perdew, Robert G. Parr, Mel Levy, and Jose L. Balduz. Density-functional theory for fractional particle number: Derivative discontinuities of the energy. *Phys. Rev. Lett.*, 49:1691–1694, Dec 1982.

[23] A.W. Sleight, H. y. Chen, A. Ferretti, and D.E. Cox. Crystal growth and structure of $BiVO_4$. *Materials Research Bulletin*, 14(12):1571–1581, 1979.

[24] Thomas D. Kühne, Marcella Iannuzzi, Mauro Del Ben, Vladimir V. Rybkin, Patrick Seewald, Frederick Stein, Teodoro Laino, Rustam Z. Khaliullin, Ole S̃chütt, Florian Schiffmann, Dorothea Golze, Jan Wilhelm, Sergey Chulkov, Mohammad Hossein Bani-Hashemian, Valéry Weber, Urban Borštnik, Mathi͂eu Taillefumier, Alice Shoshana Jakobovits, Alfio Lazzaro, Hans Pabst, Tiziano Müller, Robert Schade, Manuel Guidon, Samuel Andermatt, Nico Holmberg, Gregor y K. Schenter, Anna Hehn, Augustin Bussy, Fabian Belleflamme, Gloria Tabacchi, Andreas Glöß, Michael Lass, Iain Bethune, Christopher J. Mundy, Matt Plessl, Christian an d Watkins, Joost VandeVondele, Matthias Krack, and Jürg Hutter. Cp2k: An electronic structure and molecular dynamics software package - quickstep: Efficient and

accurate electronic structure calculations. *The Journal of Chemical Physics*, 152(19):194103, 05 2020.

[25] Joost VandeVondele, Matthias Krack, Fawzi Mohamed, Michele Parrinello, Thomas Chassaing, and Jürg Hutter. Quickstep: Fast and accurate density functional calculations using a mixed gaussian and plane waves approach. *Computer Physics Communications*, 167(2):103–128, 2005.

[26] Stefano Falletta and Alfredo Pasquarello. Polarons free from many-body self-interaction in density functional theory. *Phys. Rev. B*, 106:125119, Sep 2022.

A

Python scripts

A.1 supercell.py

```
from ase.io import read, write
from ase.build import make_supercell

# Load the structure from the CIF file
structure = read("bivo.cif")

# Define the transformation matrix for the supercell
# This is an example 3x3 matrix; replace it with the matrix you need
transformation_matrix = [[2, 0, 0],
                         [0, 2, 0],
                         [0, 0, 2]]

#[[2, -2, 0], for rotated cell
#[2, 2, 0],
#[0, 0, 1]]

# Create the supercell using the matrix
supercell = make_supercell(structure, transformation_matrix)

# Write the supercell to a new CIF file
write("bivo_supercell-192.xyz", supercell, format='extxyz',
      columns=['symbols', 'positions'])


print("Supercell created and saved as 'bivo_supercell.xyz'")
```

A.2 cell.py

```
import os
# Define the input .xyz files and the corresponding output files
file_mapping = {
    "bivo_supercell-192-surface.xyz": "cell-192-surface",
    "bivo_supercell-192.xyz": "cell-192",
#    "bivo_supercell-384.xyz": "cell-384"
}

def extract_and_save_cell_size(input_file, output_file):
    with open(input_file, 'r') as file:
        lines = file.readlines()
        # The second line contains the lattice parameters
        lattice_line = lines[1]

        # Extract the Lattice parameter values
        if "Lattice=" in lattice_line:
            lattice_string =
                lattice_line.split('Lattice="')[1].split('"')[0]
            lattice_values =
                [float(value) for value in lattice_string.split()]

            # Format the lattice vectors
            A = lattice_values[0:3]
            B = lattice_values[3:6]
            C = lattice_values[6:9]

            # Prepare the content for the output file
            cell_data = (f"A [angstrom] {A[0]} {A[1]} {A[2]}\n"
                         f"B [angstrom] {B[0]} {B[1]} {B[2]}\n"
                         f"C [angstrom] {C[0]} {C[1]} {C[2]}\n")

            # Write the cell data to the corresponding output file
            with open(output_file, 'w') as output:
                output.write(cell_data)
            print(f"Cell data saved to {output_file}")
        else:
            print(f"Lattice information not found in {input_file}")

# Iterate over the file mappings and extract cell sizes
for input_file, output_file in file_mapping.items():
    if os.path.exists(input_file):
        extract_and_save_cell_size(input_file, output_file)
    else:
        print(f"File {input_file} not found.")
```

B

CP2K input file

```
@SET XYZNAME    ./bivo_supercell-192.xyz
@SET PROJNAME   192-supercell
@SET HF_FRAC    0.14
@SET SL_FRAC    0.86


&GLOBAL
PROJECT      ${PROJNAME}
RUN_TYPE     GEO_OPT
PRINT_LEVEL  MEDIUM
WALLTIME     23:58:00
&END GLOBAL

&FORCE_EVAL
        METHOD         Quickstep
        STRESS_TENSOR  NONE
        &PRINT
        &END PRINT
        &DFT
                LSD
                MULTIPLICITY 3
                BASIS_SET_FILE_NAME     BASIS_MOLOPT
                POTENTIAL_FILE_NAME     GTH_POTENTIALS
                BASIS_SET_FILE_NAME     BASIS_ADMM
                BASIS_SET_FILE_NAME     BASIS_ADMM_MOLOPT
                &MGRID
                        CUTOFF       800
                        REL_CUTOFF    80
                &END MGRID
                &QS
                        EPS_PGF_ORB  1.0E-20
                        METHOD GPW
                        EXTRAPOLATION ASPC
                &END QS
                &AUXILIARY_DENSITY_MATRIX_METHOD
                        METHOD BASIS_PROJECTION
                        ADMM_PURIFICATION_METHOD MO_DIAG
```

```
            &END AUXILIARY_DENSITY_MATRIX_METHOD
            &SCF
                    SCF_GUESS  RESTART
                    EPS_SCF    5.0E-7
                    MAX_SCF    50
                    &OT
                            MINIMIZER       CG
                            PRECONDITIONER  FULL_SINGLE_INVERSE
                    &END OT
                    &OUTER_SCF
                    EPS_SCF  5.0E-7
                    MAX_SCF  10
                    &END OUTER_SCF
            &END SCF
            &XC
                    &XC_FUNCTIONAL
                            &PBE
                                    SCALE_X ${SL_FRAC}
                                    SCALE_C 1.0
                            &END PBE
                    &PBE_HOLE_T_C_LR
                            CUTOFF_RADIUS 5.0
            SCALE_X ${HF_FRAC}
                    &END PBE_HOLE_T_C_LR
                    &END XC_FUNCTIONAL
                    &HF
                            &SCREENING
                                    EPS_SCHWARZ 1.0E-6
                                    SCREEN_ON_INITIAL_P FALSE
                            &END SCREENING
                            &INTERACTION_POTENTIAL
                                    POTENTIAL_TYPE TRUNCATED
                                    CUTOFF_RADIUS 5.0
                                    T_C_G_DATA t_c_g.dat
                            &END INTERACTION_POTENTIAL
                            &MEMORY
                                    MAX_MEMORY 1700
                                    EPS_STORAGE_SCALING 0.1
                            &END MEMORY
            FRACTION ${HF_FRAC}
                    &END HF
            &END XC
    &PRINT
        &V_HARTREE_CUBE
            &EACH
                GEO_OPT     0
```

```
        &END EACH
        ADD_LAST    SYMBOLIC
    &END V_HARTREE_CUBE
    &MO_CUBES
        NHOMO 1
        NLUMO 1
        WRITE_CUBE T
        &EACH
            GEO_OPT 1
        &END EACH
    &END MO_CUBES

    &PDOS
        &EACH
            GEO_OPT     0
        &END EACH
        ADD_LAST    SYMBOLIC
        NLUMO       -1
        COMPONENTS
    &END PDOS
&END PRINT
&END DFT
&SUBSYS
        &CELL
                @INCLUDE 'cell-192'
        &END CELL
        &TOPOLOGY
                COORD_FILE_NAME   ${XYZNAME}
                COORD_FILE_FORMAT xyz
        &END TOPOLOGY
        &KIND Bi
                BASIS_SET         DZVP-MOLOPT-SR-GTH-q5
                BASIS_SET AUX_FIT cFIT6
                POTENTIAL         GTH-PBE-q5
        &END KIND
        &KIND O
                BASIS_SET         DZVP-MOLOPT-SR-GTH-q6
                BASIS_SET AUX_FIT cFIT3
                POTENTIAL         GTH-PBE-q6
        &END KIND
        &KIND V
                BASIS_SET         DZVP-MOLOPT-SR-GTH-q13
                BASIS_SET AUX_FIT cFIT10
                POTENTIAL         GTH-PBE-q13
        &END KIND
&END SUBSYS
```

```
&END FORCE_EVAL

&MOTION
        &GEO_OPT
                MAX_FORCE [eV*angstrom^-1] 0.01
        &END GEO_OPT
        &PRINT
                &TRAJECTORY
                        &EACH
                                GEO_OPT 1
                        &END EACH
                &END TRAJECTORY
        &END PRINT
&END MOTION
```